Università degli Studi di Padova

DIPARTIMENTO DI INGEGNERIA INDUSTRIALE
Corso di Laurea Magistrale in Ingegneria Aerospaziale

Tesi di laurea magistrale

A CFD-based approach for cavitating geometries.

Candidato:
Eugenio Bellon
Matricola 1155504

Relatore:
Ch.mo Prof.Ernesto Benini

Anno Accademico 2018–2019

Contents

List of Figures

List of Tables

1 Introduction

The aim of this thesis is to study and to numerically simulate the cavitation phenomenon in order to understand how supercavitation can be realized so as to minimize the drag of an underwater body.
Supercavitation has been historically used for war reasons, but today it is studied for the great advantages that it can also bring in the civil field. This technology envelopes underwater vessels with a large bubble, allowing them to travel even at supersonic speed [13]. The VA-111 Shkval torpedo was the first supercavitating underwater vehicle and it was developed by Soviet Union during the cold war. Through this technology, it was capable of reaching speeds of more than 370km/h [14].

Figure 1.1: A detail of the VA-111 Shkaval

It was possible just because there was a drag reduction which enabled such a good efficiency to be reached, then understanding why this drag reduction occurs is the basis of this study. It is consequently important to propose a computational setup to predict the exact behaviour of cavitating fluids, so it is for this reason we will

present and validate a CFD (computational fluid dynamics) model.
Thanks to this work, we can discover the intimate nature of cavitation and we can unlock secrets to supercavitation.
In particular, we will answer these questions:

- is it possible to establish supercavitation starting at v=0m/s?
- are there any possible developments on the model that can be made?
- what are the further potentials to be developed in a future work?

2 Cavitation

"*Cavitation is a phenomenon in which rapid changes of pressure in a liquid create vapor-filled cavities, in places where the pressure is relatively low*" [14]. There is a pressure threshold below which cavitation occurs and it is strictly related to the microscopic scale properties of the medium. In spite of that, the approach will be towards macroscopic fluid scales because they have a more relevant meaning in the purpose to offer practical solutions for industrial systems.
Once pressure has reached this value, a phase transformation from liquid to vapour happens. This is due to a pressure drop, unlike boiling in which it is due to a temperature rise (figure 2.1).
To a first approximation, P_v (Vapour Pressure) is the value for which cavitation

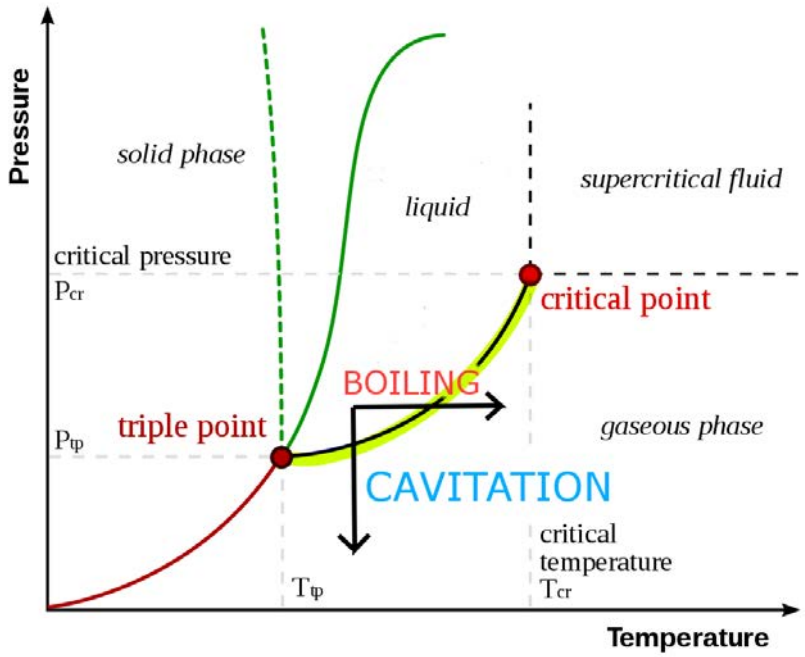

Figure 2.1: Phase Diagram

starts and it is highlighted in green. As can be seen it is a function of the temperature T.

The phase change is not only related to vapour pressure, indeed lower pressures could be reached. This defines another variable that is the static delay: it is the difference between p_v and the pressure at which cavitation begins.

In the first instance the heat required for the formation of vapour is negligible so it can be assumed that cavitation is an isothermal transformation.

It could be divided into three steps [1]:

- creation of voids;
- filling voids with vapour;
- vapour saturation.

These steps are so fast that they could be assumed as one. Nevertheless, these

time variations are very important theoretically and computationally because they influence the field of motion itself.
When a quasi-steady equilibrium is reached, three different structures could be recognized [1]

- transient isolated bubbles: they appear and immediately disappear because they are filled by a small amount of gas. They are first carried along by the main flow in a low pressure area and subsequently disappear when they enter areas of high enough pressure. This is what happens in a Venturi nozzle;

- attached cavities: they are the ones which this thesis is more interests in, indeed they are the typical structures that appear in supercavitation (figure 2.2). They are stable cavities and they are usually attached to the leading edge of the bodies;

- cavitating vortices: they appear in the low-pressure core of vortices in turbulent wakes; these structures are typical of 3D wings and propeller blades.

The aim of this project is to design a geometry that enhances cavitation, in order to create stable cavity (attached cavity) as soon as possible for the reasons set out in the first chapter. In order to do this we need to emphasize the pressure drop.
Sharp edges create a local velocity increase. The more the speed increases the greater the pressure drop (Bernulli's equation):

$$p + \frac{\rho v^2}{2} + \rho g h = c$$

Even if they are not presented here, there are a lot of problems related to cavitation: production of noise, vibrations and wall erosion. These are the reasons why

Figure 2.2: Supercavitating Sphere

cavitation is studied as a really bad condition in mechanics courses, but they won't be treated in this thesis.

2.1 Cavitation Nuclei

The cause of cavitation are voids in the medium, called cavitation nuclei that will be investigated in this section [1]. These micro-bubbles are present in the liquid medium.

Their evolution does not only depend on vapour pressure because they can withstand lower pressures. That is why we introduced static delay in the previous chapter.

These radius R microbubbles (figure 2.3) are immersed in a liquid, and they are characterized by S, surface tension, p_∞, pressure outside the bubble, p_g and p_v, respectively the vapor pressure and the pressure of the gas contained in it. Assuming that R is small and the difference in hydrostatic pressure is negligible, the equilibrium of interface between the two mediums is guaranteed by the following equation [1]

$$p_\infty = p_g + p_v - \frac{2S}{R}$$

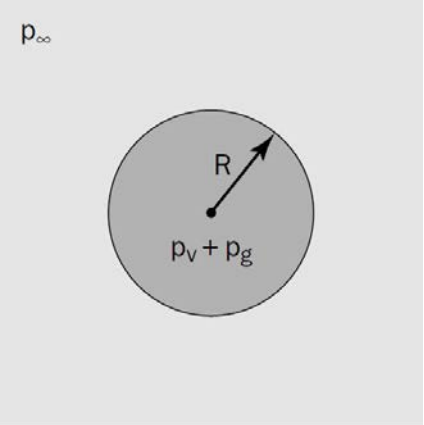

Figure 2.3: Sphere Micro Bubble

We want to study how the pressure varies in relation to the bubble radius. We consider a transformation that is isothermal and in which the diffusion through the interface can be neglected because the time scales of the two phenomena are not comparable.

Considering that the gas pressure is inversely proportional to the volume and denoted an initial state 0, we can write the following relation:

$$p_\infty = p_{g0}(\frac{R_0}{R})^3 + p_v - 2\frac{2S}{R}$$

It can be seen that two terms are deeply in contrast: the gas pressure tends to increase the bubble radius while the surface tension acts to contrast this bubble growth. We can then define two points that represent two minima for pressure and radius:

$$R_c = R_0\sqrt{\frac{3p_{g0}}{2S/R_0}}$$

$$p_c = p_v - \frac{4S}{3R_c}$$

They will be treated as a line of separation between the stable and unstable conditions of the microbubbles. Indeed, it is proven [1] that the bubble starts to grow,

temporarily lowering the pressure around it. If the pressure does not reach p_c (i.e. $R < R_c$), bringing the system back to the initial condition will cause the bubble to return to the initial radius. If instead it reaches p_c (i.e. $R = R_c$), the bubble will continue to grow at even higher pressures following the right branch of the graph (figure 2.4). The minimum point of pressure is one of the most important

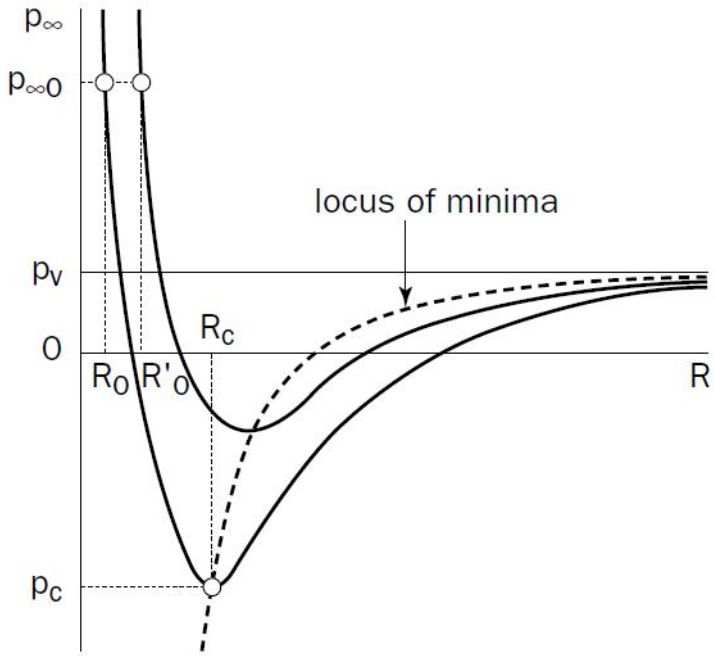

Figure 2.4: Pressure-Radius Diagram

values that has to be considered in CFD. This value will depend on the size of micro-bubbles. In the following diagram (figure 2.5) it is described how the nuclei radius affects the pressure delay under known conditions. Once fixed a radius, it is evident that higher p_∞ will correspond to lower static delays. Then if the liquid presents great bubbles it will naturally tend to cavitate. Vice versa, fixed p_∞ the smaller the bubbles will be the more the static delay will grow, making the cavitation more difficult:

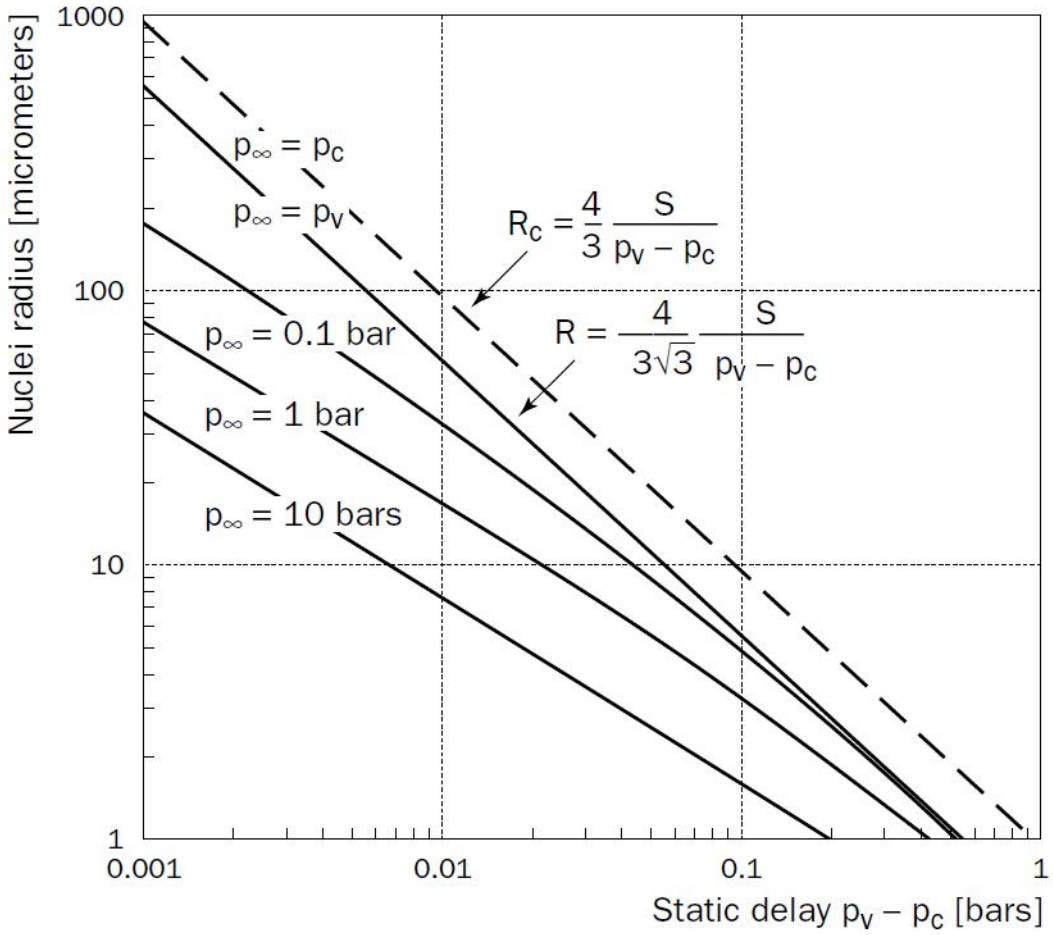

Figure 2.5: Nucleus radius - Static Delay at different p_∞

2.2 Bubble Dynamics

Knowing the evolutionary aspects of cavitation nuclei is fundamental. This allowed us to set the temporal parameters used in the simulations.

The hypotheses that have been made are:

- the liquid is incompressible, Newtonian and inviscid;
- gravity is negligible;
- the bubble is adiabatic;

- the bubble is saturated with vapor.

The basic equations of the analysed model, are those of Rayleigh-Plesset, obtained below. The flow is irrotational and the mass conservation for inviscid fluid $\nabla \cdot V = 0$ gives [1]:

$$u(r,t) = \dot{R}\frac{R^2}{r^2}$$

Where R is the radius of the bubble and $\dot{R}$ is the growth rate. In this particular case the viscous terms are also null, therefore:

$$\frac{\partial u}{\partial t} + u\frac{\partial u}{\partial r} = -\frac{1}{\rho}\frac{\partial p}{\partial r}$$

replacing the first in the second:

$$\ddot{R}\frac{R^2}{r^2} + 2\dot{R}^2[\frac{R}{r^2} - \frac{R^4}{r^5}] = -\frac{1}{\rho}\frac{\partial p}{\partial r}$$

and integrating:

$$\frac{p(r,t) - p_\infty}{\rho} = \ddot{R}\frac{R^2}{r} + 2\dot{R}^2[\frac{R}{r} - \frac{R^4}{4r^4}]$$

in the interface r=R:

$$\frac{p(R,t) - p_\infty(t)}{\rho} = R\ddot{R} + \frac{3}{2}\dot{R}^2$$

then, knowing that:

$$\frac{\partial u}{\partial r} = -\frac{\dot{R}^2}{R}$$

is found:

$$\rho[R\ddot{R} + \frac{3}{2}\dot{R}^2] = p_v - p_\infty + p_{g0}(\frac{R_0}{R})^{3\gamma} - \frac{2S}{R} - 4\mu\frac{\dot{R}}{R}$$

Setting the temporal variation of p_∞ defines also the evolution of the bubble radius. This equation will be used to determine the time parameters.

2.2.1 Bubble Collapse

In this section we will identify a characteristic time τ called Rayleigh time, that will be used in our simulations.
It is assumed that at time t=0 there is a $p_\infty > p_v$. This increase in pressure causes a shrinkage of the bubble that can be computed using the Rayleight-Plesset equation [1]:

$$\frac{dR}{dt} = -\sqrt{\frac{2}{3}\frac{p_\infty - p_v}{\rho}[\frac{R_0^3}{R^3} - 1]}$$

This allows to calculate the velocity of the interface as a function of time.
The characteristic time of collapse is defined when R=0, namely when the bubble collapses. From integration between initial radius R and final radius 0, it is possible to define the following relation:

$$\tau = 0.915 R_0 \sqrt{\frac{\rho}{p_\infty - p_v}}$$

The evolution of the bubble until the collapse is described by:

$$\frac{R}{R_0} = 1.87[\frac{\tau - t}{\tau}]^{2/5}$$

In figure below it is possible to see the trends of the graphs $R - t/\tau$ and $R - t/\tau$.

2.2.2 Nucleus Growth

Assuming now to start from known conditions, at a time t=0 there will be a rapid drop in p_∞. The sudden drop in pressure causes the gas contained in the bubble to expand. As seen in the previous chapter, you can define a law of the type $R^2 = f(R)$. You will have an opposite behaviour with respect to the previous one with two possible cases:

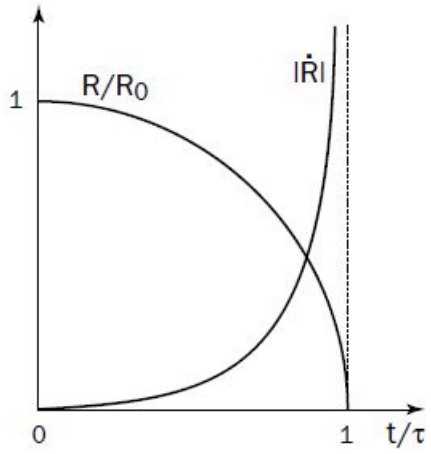

Figure 2.6: Time evolution of a bubble.

- if $f(R)$ has a root $R_1 > R_0$, the bubble will oscillate between the two values while $\dot{R}$ will change sign for $R = R_1$ and $R = R_0$. According to the ratio R_1/R_0, there will be a periodical behaviour for values of the ratio near 1 and a strong non-linear behaviour moving away from this value;

- if $f(R)$ has no roots greater than R_0 the bubble will continue to grow indefinitely.

2.3 Partial Cavities

It will now be introduced what cavities are, moving to a larger scale of the phenomenon.
First of all it is essential to define σ_c [2]:

$$\sigma_c = \frac{p_\infty - p_v}{\frac{1}{2}\rho V_\infty^2}$$

This dimensionless value is closely related to the type of flow and it will be the basis of all future formulations. There is a threshold between partial cavitation and

supercavitation (the two main stages) that in this thesis will be set as $\sigma_c = 0.1$.
Partial cavitation is the first type presented. Unlike supercavitation, it is an extremely unstable phenomenon.
For this reason, from a theoretical point of view, it is described more qualitatively than quantitatively.
The most interesting aspects are the cavitation patterns. In order to analyze these structures we used the figure 3.24, which presents different cavitating conditions. We can divide it into three zones [1]:

- non cavitating or cavitation on the lower side. This area is characterized by high σ_c or negative angles of attack;
- supercavitation. This is characterized by very high angles of attack or very low σ_c;
- partial cavitation. This is the zone we are more interested in and which is predominant in the graph for the range that our study will concern ($\sigma_c = 0 - 0.4$).

  Two types of cavities have been mainly recognized. :

  - small and stable cavities for small angles of attack and small σ_c values;
  - thicker and generally more unstable cavities for large values of angle of attack and large σ_c values.

2.3.1 Re-entrant Jet

To understand how these patterns form the re-entrant jet has to be introduced, in order to present the main characteristic of this cavity.
The minimum pressure point inside the cavity causes the fluid to deflect inside the

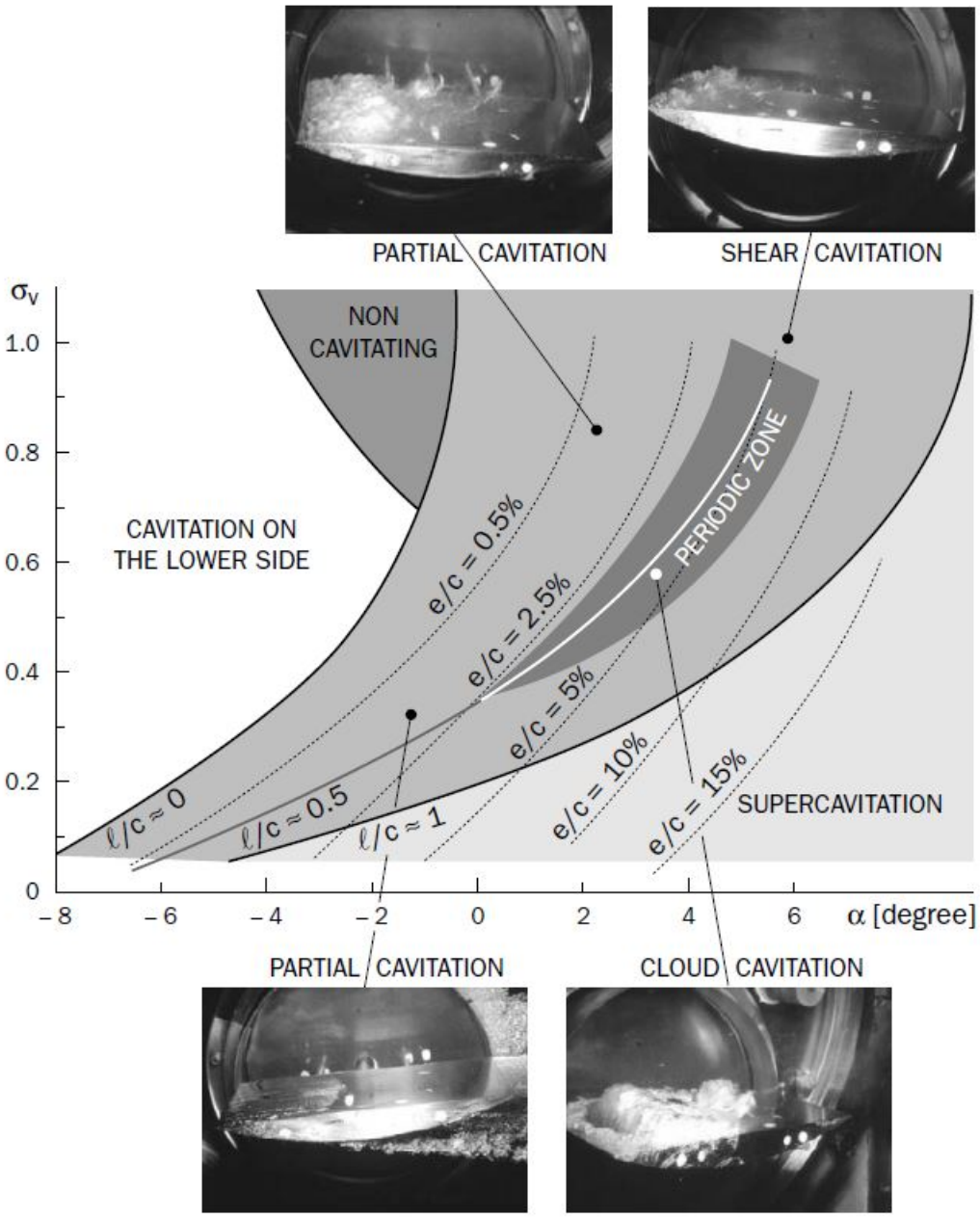

Figure 2.7: Cavitation Patterns.

bubble.
The cavity then divides the liquid in two parts [1]:

- a re-entrant jet that travels in the opposite direction of the fluid and carries small amounts of liquid;
- the fluid on the outside that reattaches to the wall.

While for small cavities this only represents an increase in pressure at the end of the bubble, for large cavities this flow can re-enter to the beginning of the cavitation bubble.
This causes a collapse of the bubble that subsequently tends to reform thanks to the pressure field. It will be seen that the phenomenon will present random aspects and periodical aspects.

2.3.2 Stable and Random Cavitation

The laws that determine the length of the cavity depend on the specific type of body.
This can be stable or unstable depending on the cavitation number and on the investigated geometry.
In the case of hydrofoils the angle of attack and the σ_c contribute to the definition of the fluid state. In general, for low sigma values (excluding supercavitation), i.e. lower than 0.4, it is evident that the fluid tends to instability.
In the opinion of the author, defining a law for the cavity length for this case is hazardous.

2.3.3 Cloud Cavitation

It is vital for this project to deal with cloud cavitation. Indeed, between the most unstable and the least unstable regime there is a transition zone in which a

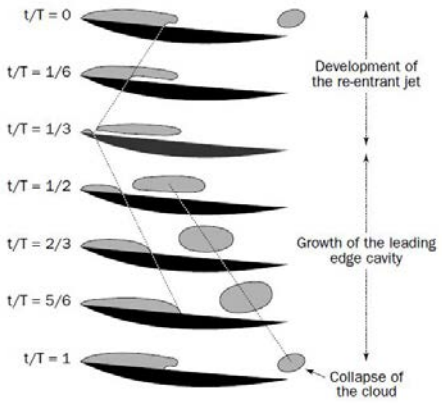

Figure 2.8: Cloud cavitation on a hydrofoil.

periodic growth and decrease of the bubble are evidenced.

The consequence is that it is not very significant to study laws to understand the length for the specific case. Conversely, approaching the description of the periodic behavior of the fluid allows us to relate it to other phenomena, such as the vortices of Von Karman [1].

A formulation of the cloud cavitation at this point is necessary, both for future testing of the CFD model with an extremely complicated task and for the study of this fascinating phenomenon.

A typical evolution of the bubble during a period of oscillation around a hydrofoil is shown in figure 2.8. The re-entrant jet flows upwards and separates the bubble in 1/3 of the period. The speed of the jet can be defined by the formula:

$$V = V_{\infty}(1 + \sigma_v)$$

As far as the period is concerned, this is defined by the Strouhal number.

This is connected to the time required to the jet to cover the length l.

Once defined a Strouhal number, experimentally comprised between 0.25-0.30

[1], the frequency of oscillation could be defined as

$$f = \frac{S V_\infty}{l}.$$

while the thickness of the jet varies between 15% and 30%.

2.3.4 Shear Cavitation in Wakes

For high Reynolds numbers the turbulent boundary layer causes cavitation to develop in the turbulent shear flow. In particular, in the wake of the studied geometries the structures observed by Belahadjii et al.[1] could be recognized. The vortices due to the shear flow in the boundary layer can be divided into two structures [1]:

- the near-wake, whose length is about 0.7d, where d is the geometry diameter;
- the far wakes that can be described by the classic vortices of Bernard-Karman.

A transition zone between the two is visible as well, in which the near-wakes evolve into Bernard-Karman vortices (figure 2.9). This will be studied later in this thesis.

2.4 Supercavitation

As soon as the cavitation number falls below a certain value, the bubble starts to grow more and more. This leads to the existence of a long vapor phase bubble, which induces considerable advantages in terms of drag reduction. For example, in hydrofoils the extra-dos will be completely wrapped in vapor, while the lower part will be wrapped in water.

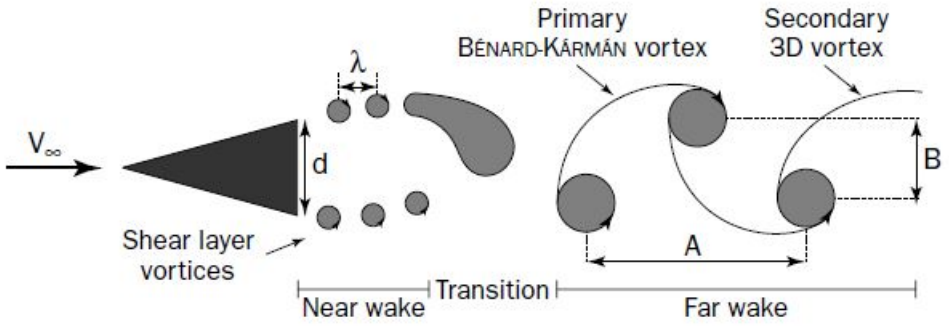

Figure 2.9: Structures due to shear layer vortices

For the purpose of foiling, this is a very interesting result. It is sufficient to consider that a reduction in density of factor 1000 can result in a drastic increase in lift, resulting in an increased efficiency. Conversely, in case of a submarine, moving on a low-density fluid translates into an strong reduction in drag.
Three are the characteristics presented in this phase [1]:

- detachment point;
- cavity closure;
- cavity length.

2.4.1 Detachment Point

There are two criteria to determine the fluid detachment [1], obviously in the case in which there is no geometric discontinuity:

- Villat-Armstrong criterion: the cavity must come off tangentially, otherwise the conditions of constant pressure and speed along a streamline cannot be maintained.

  The detachment zone for this theory is that of minimum pressure, which is calculated using an iterative method. However, this model does not take

into account the fact that the fluid is not inviscid and is thus used as a first approximation;

- Laminar Separation criterion: From the Arakeri and Acosta studies [1] it was found that viscous effects are predominant in cavitation inception. They have also proven that the local effects of surface tension impede the tangential separation.

  In practice, the existence of a laminar separation zone is the only case that allows the fluid to supercavitate, in that it creates a dead zone in which the fluid is allowed to remain attached to the surface.

  This aspect has been fundamental in order to properly interpret the simulation results. Indeed, if the boundary layer becomes turbulent, the cavity can no longer remains attached, drastically changing its characteristics. The point of laminar separation is therefore close to the point of bubble formation and the distance between them is due to surface tension.

2.4.2 Cavity Closure

The cavity pressures will always be lower than the external pressures, these force the fluid to flow inside the bubble [1].
This is clearly shown from the Euler equation:

$$\frac{V^2}{R}\mathbf{n} = -\frac{1}{\rho}\mathbf{grad}p$$

The behaviour at the closure is very similar to partial cavitation: the pressure drop creates a re-entrant jet, however the fluid never penetrates deep into the bubble.
This will create two phases [1] that alternates:

- the re-entrant jet develops and confines the bubble gas and vapor inside;

- small emissions of vortices carry with them gas and excess liquid.

2.5 Cavity Length

The cavity length increases as the number of cavitations decreases.
It has been experimentally seen that the length of cavities at low σ_c can be approximated by empirical law [1]:

$$\frac{l}{c} = A\sigma^{-n}$$

where c is a characteristic length, and A is a parameter that depends on the shape of bodies. As for n, this depends on the water depth and in this thesis will always be placed equal to one [1].
These computationally verified formulas are fundamental to design supercavitating geometries.

3 Multi-phase CFD analysis of natural cavitation

A multi-phase CFD method has been used to validate and model the flow around a hemispherical head. The purpose is to find an accurate and efficient solution in terms of computational cost.

This thesis is based on the work done by H. Rouse and J.S. McNown [5] in 1948: they studied the pressure distribution around different heads, using the water tunnel located at Iowa Institute of Hydraulic Research.

They tested various shapes using interchangeably head, assembled at the end of a fixed shaft. The diameter of the heads and the shaft was $25,4mm$.

Experimental data were provided by 24 piezometers mounted as shown in figure 3.2; They studied three types of geometry with different head shapes:

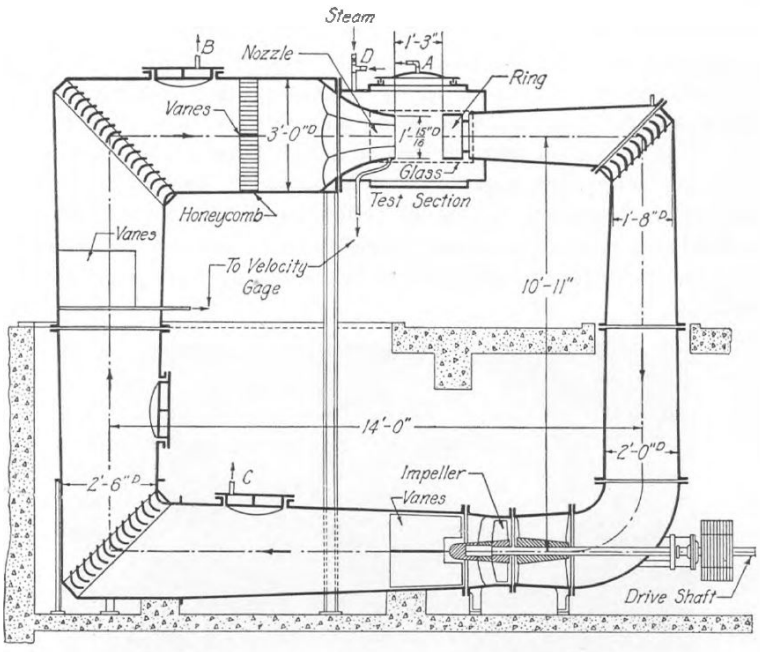

Figure 3.1: Water Tunnel - Vertical Section

- Rounded Series

- Conical Series
- Ellipsoidal Series

In the first part of this thesis rounded series will be investigated. Particularly, hemispherical head that represents the best choice for the purpose of this work. Following the results of Yang, Xiong, Guo, [2] the water conditions of the experimental setup were found in terms of viscosity, temperature and vapor pressure.
In order to do that $Re = 5.5E + 05$ was related to $\sigma = 0.4$ (Yang, Xiong, Guo). This led to define an operating temperature of $293.15K$, a water viscosity of $0.001001kg/m^2$ and a vapor pressure of $2329Pa$.
These data seemed sometimes inaccurate compared to those given by empirical formulas. For this reason the influence of different boundary conditions on the results was studied through a table not be presented here.
The choice of the length of the shaft is subjected to a reduction in the computational cost, so this have been taken arbitrarily.
As expected it did not influence the pressure coefficient that was investigated; according to Rouse and McNown the cavitation bubble appears only in the first part of the shaft for low sigma [5].
On the contrary, an overestimation of this length results in an increase in nodes and computational cost, with more instability and more time consumption.

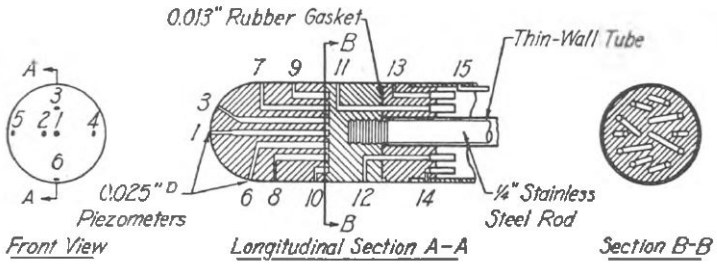

Figure 3.2: Hemispherical Head - Vertical Section

The model validation implies a lot of variables that, for a matter of time, were not all studied. This work focuses on mesh quality, mesh type, cavitation model and time-step choice.

The variables not studied have been selected by studying others' works [2, 7, 9].

The software used is Fluent.

It uses a finite volume method, and in this case it is a pressure-based solver that employs an algorithm that achieves the closure of continuity equation by solving a pressure equation, derived from the continuity and the momentum equation [14].

The solution process involves iterations that last until the convergence request is satisfied.

The pressure based algorithm is the PISO that, according to Fluent guide, is "highly recommended for all transient flow calculations" [6]. It allows to have good convergence even with large time step. This choice is fundamental for this study because a lot of tests are made with different setup.

Using a time step of 1E-05s allows the user to run simulations that are not too much time expensive. To enhance the calculation stability for this large time step, it has been used an implicit time step scheme that has no limit due to Courant-Friedrich-Lewi condition like an explicit scheme ($\sigma_c = 0.04$ implies a time step of $2.257E-06s$).

According to others' papers [7, 9] a physical time step of $1E-5s$ ensures a good transient simulation. As stated in the previous chapter the equation $\tau = 0.915R_0\sqrt{\frac{\rho}{p_\infty - p_v}}$ guarantees that a time step of $1E-5s$ is good to capture collapsing bubbles [1].

Indeed, in the last section it will be made some analysis on the transitory aspect of simulations.

3.1 Turbulence Model

The choices on the turbulence model were conducted trying to have a good trade off between computational cost and numerical results.

The simulations are intended to provide a good tool for comparing different geometries. Errors of less than 10% were accepted, provided that a more or less constant relative error was maintained.

This led to the choice of the $k - \epsilon$ model with standard wall functions (SKE). It was studied in such a way as to reduce its weaknesses.

It was also preferred to turbulence models that are able to predict the boundary layer more accurately (such as $k - \omega$ SST which was however tested) since the request for a y+ around 1 [6] would require a first cell length of 1E-05m and a growth rate of practically 1 to capture the transient phenomena of cavitation. This involves an increase in the number of nodes that in this phase of study seemed unjustified.

To obtain good results k-epsilon model needs a y+ between 30-100 to compute the boundary log layer [6].

An online calculator [11] that use the following equation:

$$y+ = \frac{yu_\tau}{\nu} \tag{1}$$

defined a first cell length of 1E-04m.

This choice has given good results. As you can see from the graph in figure 3.3 the value of y+ is always between 30 and 100.

A drop in y+ creates a zone of instability, due to the detachment and reattachment of water in the liquid phase. This instability is clearly critical to simulations, but it does not seem to influence neither the size of the cavitation bubble nor the pressure profile.

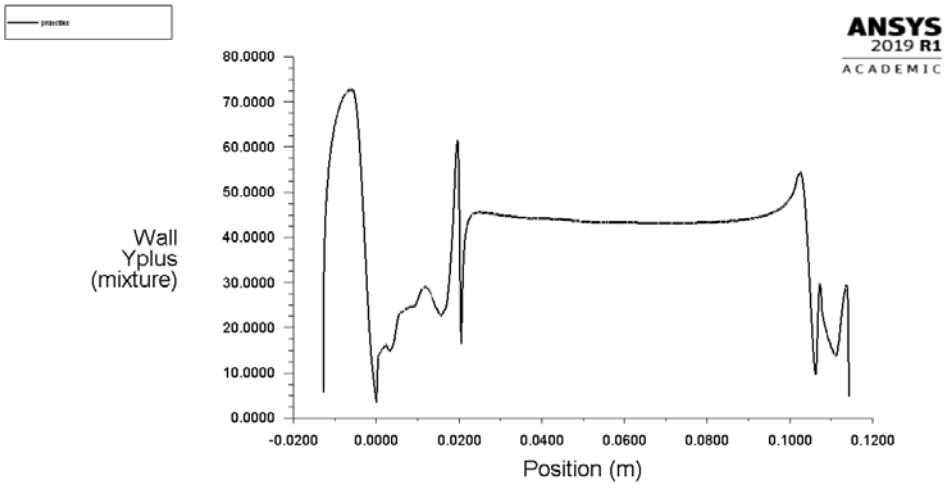

Figure 3.3: y+ plotted along the projectile curve at $t = 0.014s$ and $\sigma_c = 0.4$

At higher Re, the bubble stabilizes and y+ tends to zero in the vapor zones, in line with the physical properties of the fluid.

Another important issue is choosing the turbulence parameters at the inlet of the domain. Setting V_∞, various formulations were used both empirical [9] and theoretical [6] in order to find them.

The k epsilon terms in fact have been imposed without knowing the water tunnel turbulence conditions. We started from the turbulence intensity that we have set at 3%.

This allowed to compute the value of the turbulent kinetic energy through the following relationship [6]:

$$k = \frac{3}{2}(U_\infty I)^2$$

In this case it is 6.62E-01 m^2/s^2.

After choosing this, the real keystone was to find a suitable value for the turbulent dissipation rate (ϵ). Small variations can cause large differences in the data [6].

The method for its calculation is essentially based on the Fluent guide [6] and a

trial and error method. The advice is to follow this formula:

$$\epsilon = \frac{\Delta k U_\infty}{L_\infty} \tag{2}$$

L_∞ is a characteristic length that describes the water tunnel and we chose the length of the shaft. In addition, we must choose the Δk value but it is very difficult to have true values of the kinetic energy drop.

Different ϵ values have been tested assuming a decay between 0% and 30%; the best results have been obtained for $\Delta k = 20\%$ that corresponds to $\epsilon \approx 28 m^2/s^3$ for $\sigma = 0.4$.

It influenced pressure coefficient, bubble length and drag coefficient, the main data that were sought. This makes us understand the importance of setting this value appropriately and will certainly be analysed in the future to refine the model definitively.

3.2 Cavitation Model

Two of the three models in fluent were tested for cavitation: the Singhal et al. model and the Schnerr and Sauer model.

Both reach the convergence when residuals are $1E-04$, showing good behaviour in supercavitation studies. The Singhal proved to be more unstable in partial cavitation.

The aim is not only to validate a model for supercavitation, but a model that shows the transitional phase from non-cavitating to supercavitating conditions of submarine engines, obviously passing through a phase of partial cavitation. For this reason Schnerr and Sauer one was chosen.

First of all it is important to understand how the two-phase system will be man-

aged [6]:

$$\frac{\partial}{\partial t}(\rho_2\alpha_2) + \boldsymbol{\nabla}\cdot(\rho_2\alpha_2\mathbf{u}) = R_e - R_c$$

The model used is then briefly introduced:

if $p < p_v$,

$$R_e = \frac{\rho_1\rho_2}{\rho_m}\alpha(1-\alpha)\frac{3}{R_B}\sqrt{\frac{2}{3}\frac{p_v - p}{\rho_l}}$$

and, if $p > p_v$

$$R_c = \frac{\rho_1\rho_2}{\rho_m}\alpha(1-\alpha)\frac{3}{R_B}\sqrt{\frac{2}{3}\frac{p - p_v}{\rho_l}}$$

the volume fraction α is defined as

$$\alpha = \frac{n_b\frac{4}{3}\pi R_b^3}{1 + n_b\frac{4}{3}\pi R_B^3}$$

where n_B is the number of bubbles per volume of liquid, that is assume to 10^{14} nuclei/cm^3 [9].

3.3 Eddy-Viscosity

According to Yang et al.[2], standard turbulence models do not predict well the oscillating interface between two phases. This is essentially due to the fact that the turbulent viscosity is overestimated, particularly in the interface areas.
To avoid the problem we choose to follow the approach taken by Hanimann, Mangani, Casartelli, Widmer. A modified formulation has been adopted [12]

$$\mu_t = f(\rho)C_\mu\frac{k^2}{\epsilon}$$

$$f(\rho) = \rho_v + (\frac{\rho_v - \rho}{\rho_v - \rho_l})^n(\rho_l - \rho_v)$$

where n=10

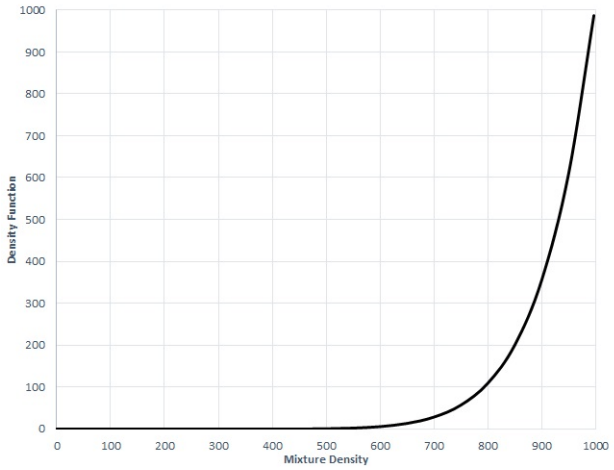

Figure 3.4: Density profile using a personal UDF to compute turbulent viscosity.

3.4 Domain

Explained the computational setup, the analysis has moved to different types of meshes, both in terms of structured and unstructured, and in size.

The dimensions of the domain were initially tested [4].

The characteristic size is the diameter of the shaft (25.4mm).

The geometry of the domain is two-dimensional and was initially studied to facilitate the creation of structured meshes: there are two semicircles connected to each other by a surface [9].

The first geometry has been dimensioned defining a radius equal to 5 times the diameter of the studied head (figure 3.5), while the second one has a radius equal to 10 times the diameter. The radii on the axis of rotation has been respectively divided in 100 nodes for the 5d geometry and in 200 nodes for the 10d geometry.

Despite what it has been said before, a common choice was adopted for the length of the first cell of 0.5mm. The criterion on the boundary layer was not met in

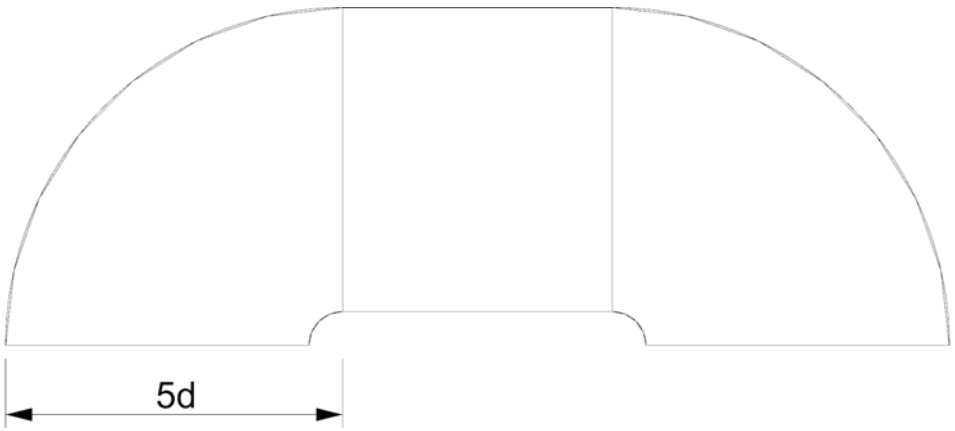

Figure 3.5: First domain that has been tested - 5d geometry

this first case, but for the purposes of simulation it does not unduly influence the considerations that can be made. The goal is to verify that the length of the bubble and the distribution of pressure results are less influenced as possible, in agreement obviously with the theory.

The dimension of the domain influences the characteristics of the fluid both physically and computatively.

In order to verify this, $1.4E + 3$ time steps have been carried out, and the average pressure distribution has been calculated within the period studied. As expected, a smaller domain, though almost imperceptibly, changes the fluid field by overestimating the length of the bubble (figure 3.6). In order to figure this out, we just see the overshoot corresponding to the increase in pressure at the end of the bubble.

The choice of the 10d domain, even if it was not a determining choice for the attainment of the validation, seemed the most suitable because it did not represent a big increase in computational cost.

Moreover as the Reynolds number increases, it is logical to expect an increase in the size of the bubble increasing the differences in results between the two domains.

In order to guarantee an independence of results from the size of the domain,

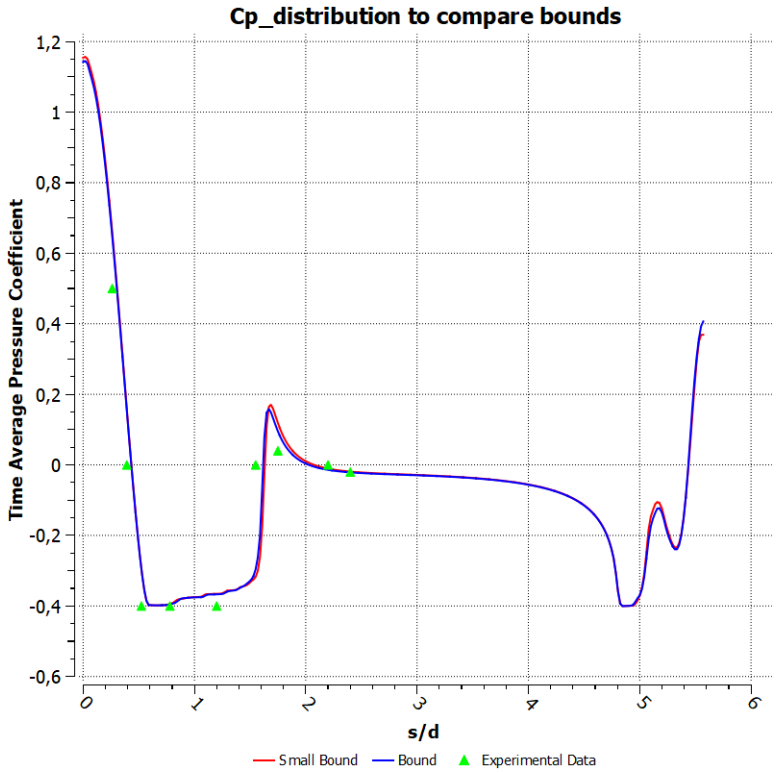

Figure 3.6: c_p comparison between the two bounds. The green triangles represents the experimental data that has been used (Rouse-Mcnown)

maintaining the ”margin” seemed to be a must.

3.5 Grid Independence

The mesh type and its quality are the main factors to obtain good results.

The common choice is selecting a type of mesh (structured, unstructured or hybrid) and perform an analysis on the independence of the solution beyond a certain degree of refinement.

Nevertheless, an analysis has been carried out for both structured and unstructured mesh because we would understand if one is better than the other to capture the strong non-stationary nature of the flow.

An unstructured mesh will finally be used.

This type of work has been carried out taking inspiration from the work done by Mansour et al [9].

3.5.1 Structured Mesh

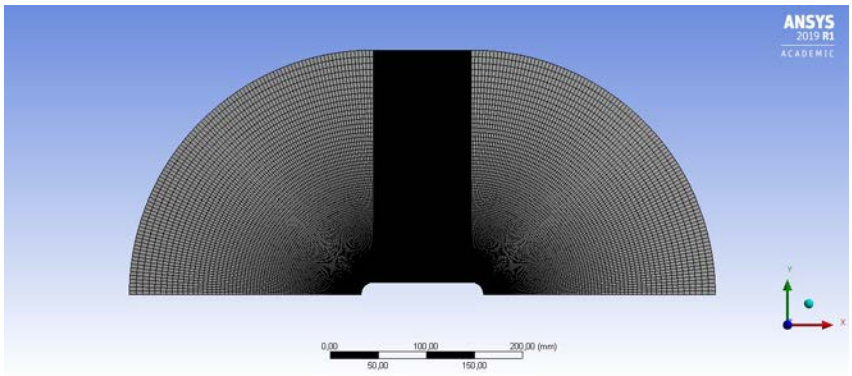

Figure 3.7: High quality structured mesh

The structured mesh was divided into 3 zones, one corresponding to the inlet, one corresponding to the body and one corresponding to the outlet. This allowed an easy control of the mesh (figure 3.5).

Two were the meshes tested: a 478x100 nodes mesh (47874) and a 713x150 (107059).

This first simulations allowed to study statically how a more or less refined mesh influenced the fluid field.

The term that we studied was the division of the head with an element of 0.2mm (high quality mesh fig.3.8) and 0.3mm (medium quality mesh), respectively. The reason why we perform these tests is the overestimation of the pressure on the profile tip caused by a coarse mesh, giving results too far from the truth, especially in terms of c_d.

Big differences between the two have not been highlighted (figure 3.9) so the 0.3mm refinement in the tip seemed sufficient.

Instead, the graph of the measured c_p (figure 3.10) is very clear; the overshoot of high resolution meshes approximates the experimental data in a more than satisfactory way in the interval 0.014s.
A more refined mesh has better results and this is not a surprise.
In fact, it approximates better the temporal behaviour of the fluid. We can expect that even the medium mesh can reach good values in the overshoot and therefore in the sizing of the bubble, but we have to perform more time steps. Studying the phenomenon we understand that this time dependence is not physical.

3.5.2 Unstructured Mesh

Was it worth using a structured meshes?
There were clear signs that using an unstructured mesh could have significant advantages:

- first of all for the ease of realization: generating structured meshes is a fairly simple process as long as you work with simple and hemispherical geometries .
  Changing the geometry complicates it because this amounts to change immediately the domain.

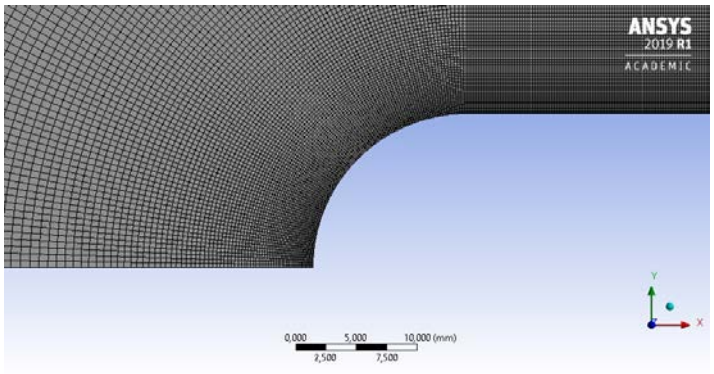

Figure 3.8: High quality mesh refinement at leading edge

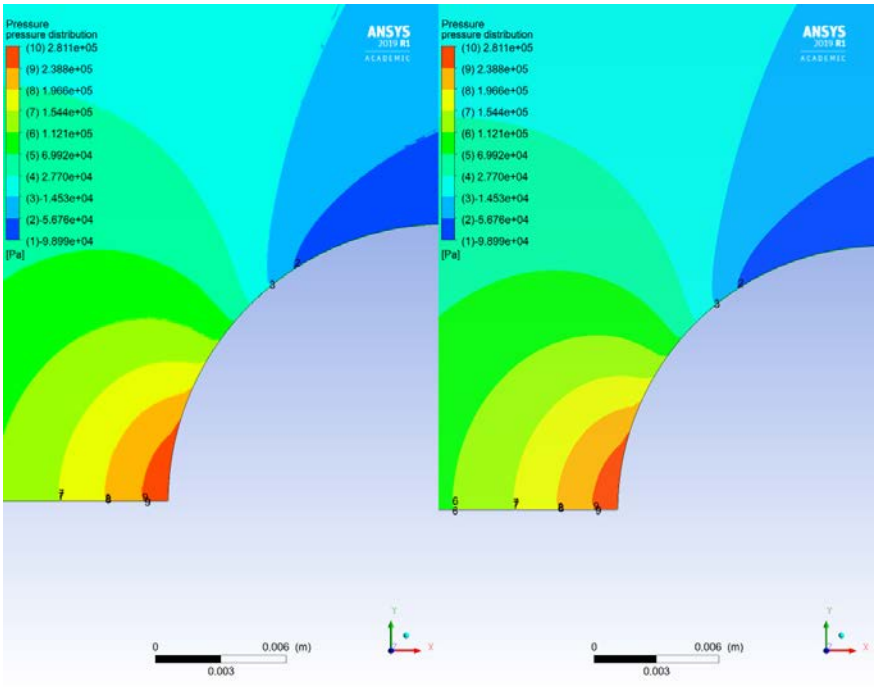

Figure 3.9: On the left side high mesh tip pressure distribution, on the right medium mesh tip pressure distritbution.

In addition, extending the model to a 3D domain would have brought into play other parameters, as well as requiring the use of other softwares;

- second, creating a very refined structured mesh around the geometry tested translates into an exponential increase in the area ratio at the far field. The cells connecting the inlet and the wallbound have huge differences (figure 3.11); a high aspect ratio creates convergence problems, which with the required residuals is not so evident. Trying to refine the model there would be major problems;

- last but not least, there are clear references in other works to the fact that an unstructured mesh is more precise in capturing the temporal aspects of the fluid (Mansour et al [9]).

  Although no definitive position has been taken on this issue, the analysis of

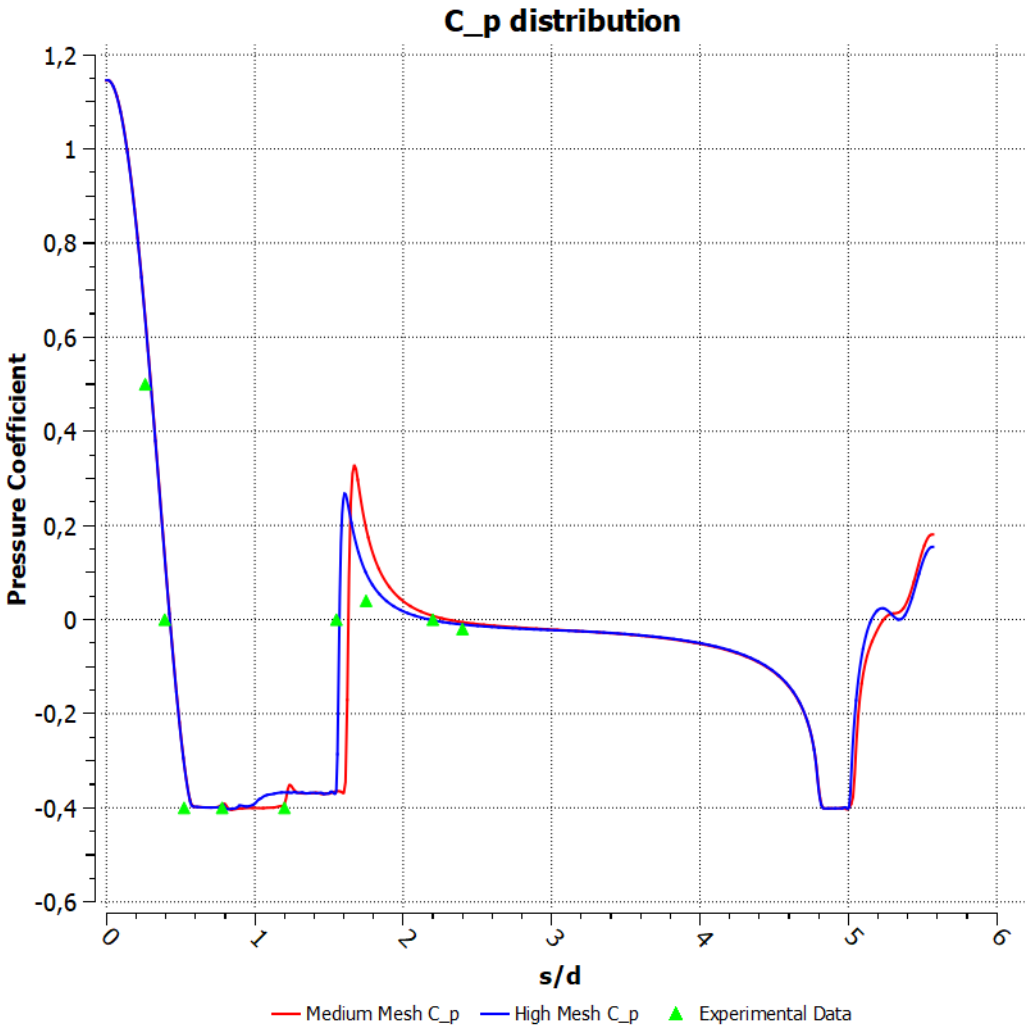

Figure 3.10: c_p distribution for the two types of mesh.

the non-stationary nature of the fluid has been performed on an unstructured mesh.

These cons were known at the beginning but it was verified the goodness of one mesh against the other through the classic study of pressure coefficients.
Modelling the unstructured mesh has focused to an unusual use of the inflation layer that will be extended to the supercavitation: a rather small cell size is required in order to predict properly the behaviour of the liquid-vapor interface.

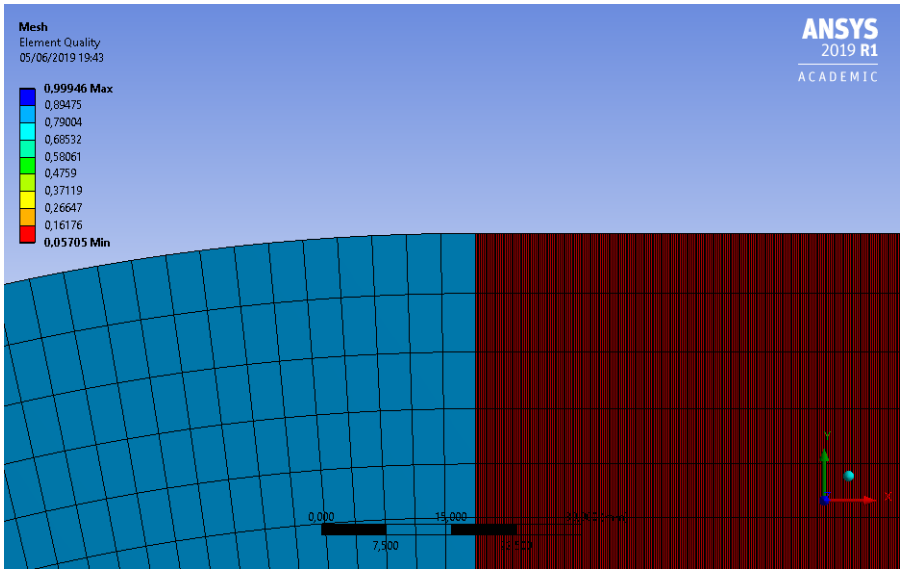

Figure 3.11: Low mesh quality between two zones, due to high aspect ratio.

The issue can be addressed in two ways:

- with a rather low growth rate, consequently increasing the nodes in areas where the flow does not have significant changes;
- creating an inflation layer that includes also the interface.

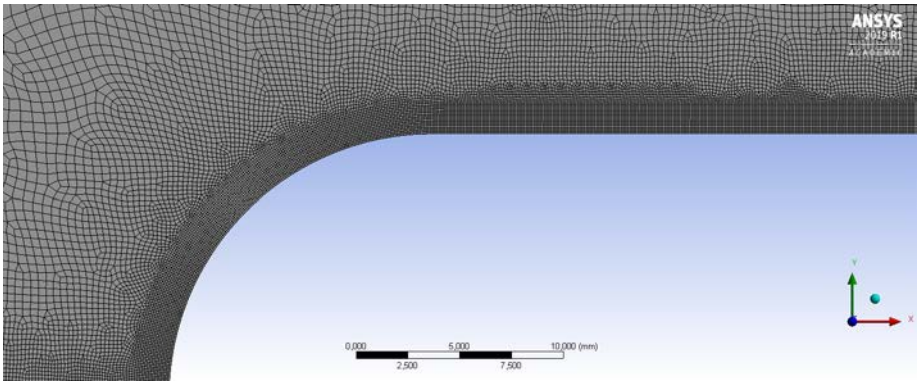

Figure 3.12: Definitive mesh with inflation layer.

After some tests, we came to the realization of the final mesh: the geometry was defined on its boundaries by cells of 0.1mm x 0.1mm while the bubble was defined

by cells of about two millimetres refined by the inflation layer, that we computed through the following equation:

$$\frac{d_c}{d} = \sqrt{\frac{c_d}{\sigma}} \tag{3}$$

Where d_c is the expected bubble diameter and c_d is computed with this formulation:

$$c_d = \frac{D}{\frac{1}{2}\rho V_\infty^2 A}$$

where A is the cross-sectional Area of the geometry.
Even if this formulation is valid for σ less than 1, it can give in first approximation an idea on the size of the bubble. Assuming $c_d = 0.45$, the bubble diameter will be $26.9mm$.
The final test was between structured and unstructured meshes. This evidences why we choose an unstructured mesh:

- the c_p averaged clearly shows better results, in terms of position of the main characteristics of the fluid (overshoot and zerocrossing) and in terms of a better prediction (lower) of the c_p on the tip (fig. 3.13).

- the practicality of developing an unstructured mesh is an aspect of fundamental importance in this study because we will perform a lot of simulations. Moreover in terms of convergence and number of nodes the choice falls on an unstructured one: 107059 vs 69222.

- as explained in the next section, the temporal behavior of unstructured mesh simulation is extremely appreciable; this was actually expected by Mansour's studies [9], and has never been questioned in this thesis, but represents a further point in favour of unstructured mesh.

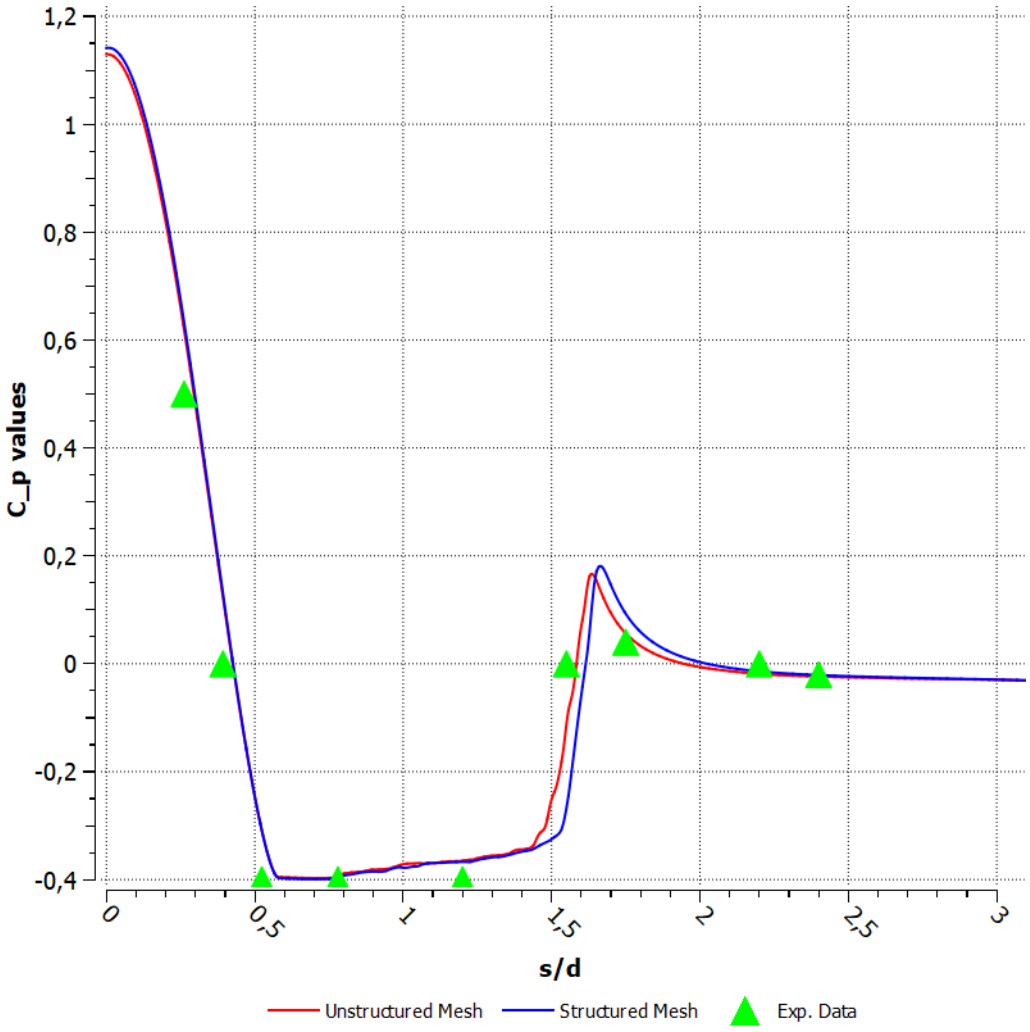

Figure 3.13: Average c_p distribution for the two best meshes.

3.6 Time Behaviour of the Model

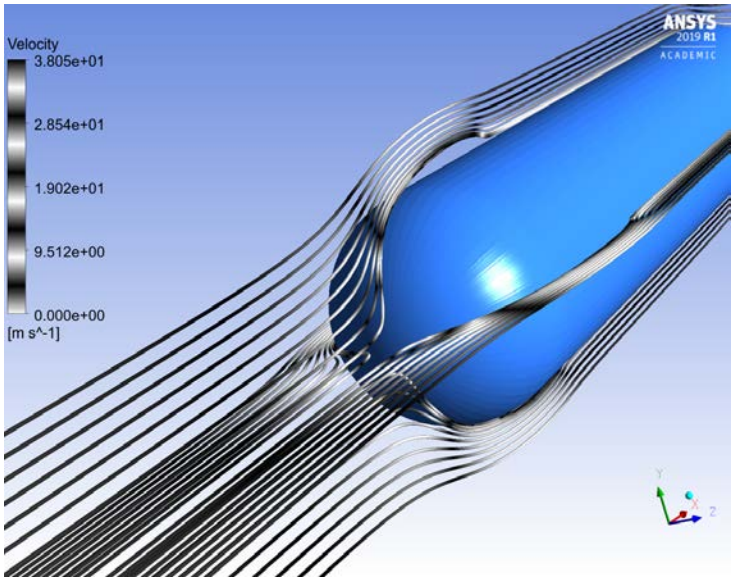

Figure 3.14: Streamline development at 5ms.

The difference between supercavitation and cavitation lies in the time instability of the solution.

Not having experimental data to compare the results, (mainly because it is really difficult to collect data) it was followed a theoretical approach in order to analyse the model and basically the type of flow studied.

We tried to understand if what come out from simulations is in line with the theory prediction. What was expected was unstable cavitation because of the high cavitation numbers. The aim of this section is to understand if some periodicity are recognizable.

3.6.1 Wake Cavitation

The presence of vortices in the wake is due to the presence of rotational structures, one of the possible causes of cavitation. These generate areas at low pressures.

In cavitation there is a substantial change in the form of these vortices:

$$\frac{d_l}{d_v} = \sqrt{\frac{\rho_v}{\rho_l}} \tag{4}$$

The diameter of the same vortices in cavitation is greater 10^3 then in non-cavitating

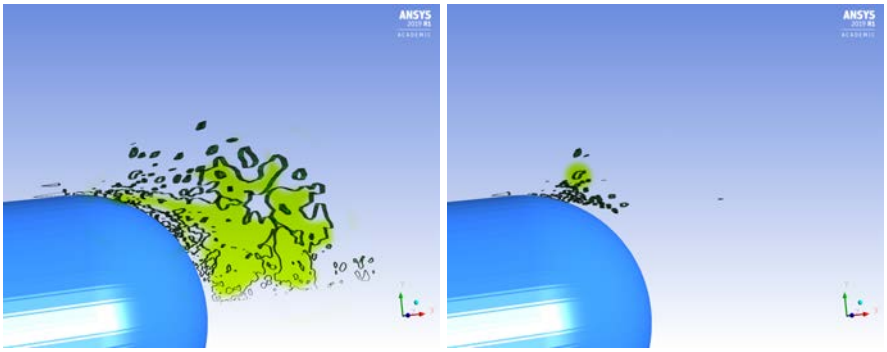

Figure 3.15: Comparison between vortices core in the wake of the body; on the left it could be seen that the diameter is much larger that one on the right. The difference stands between the fluid that composes the vortices.

condition. Indeed the model (figure 3.15) showed that the diameter of the vortices in ”cavitation mode” is huge compared than non cavitating one.

The evolution of the wake is plotted in figure 3.18. This is closely linked to two main factors: the pressure and the transition of the boundary layer. Both contribute in the separation of the flow.

If on one hand the positive gradient of pressure leads to fluid separation, on the other hand the type of boundary layer, laminar or turbulent modifies this behaviour.

The phase change is very fast at the end of the profile, in the order of 0.1ms.

As it is visible in the first two figures of 3.18, the bubble on the wake is completely developed, and it begins already to collapse in the third one. This behaviour seems in some way contradictory: if the flow remains attached, pressures should increase not allowing the cavitation, if the flow detaches there must be an explanation why

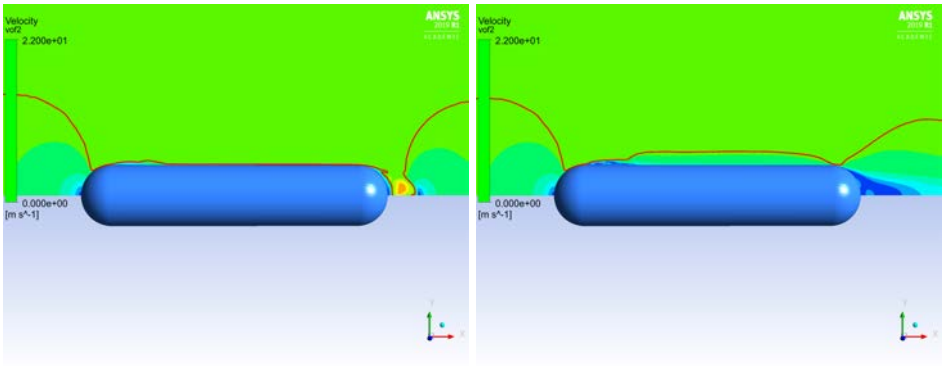

Figure 3.16: On the left: flow reattachment at 1ms; On the right: boundary layer transition.

it does not cavitate in the wake.

In order to understand this, we decided to study the thickness of the boundary layer at $1ms$ and $12ms$ respectively. We decided to analyse the value of δ_{99} (boundary layer thickness, in figure 3.16 the red line) that is where the speed of the fluid is $0.99V_\infty$ (in the case studied $21.93m/s$). The turbulent boundary layer is much more resistant to separation due to pressure gradients, as we know.

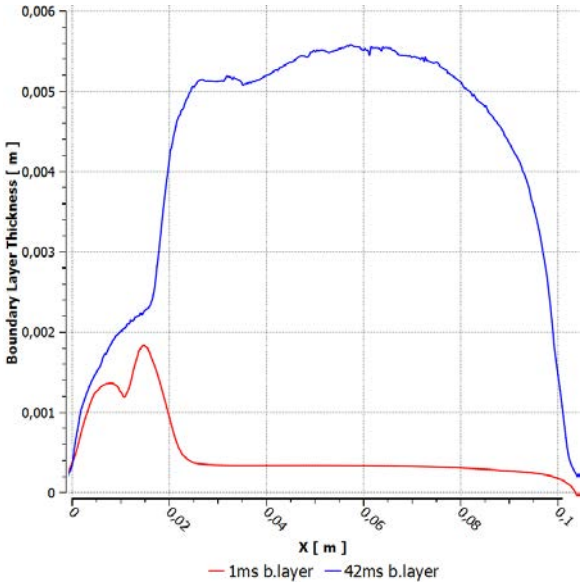

Figure 3.17: Boundary layer comparison between two different time steps.

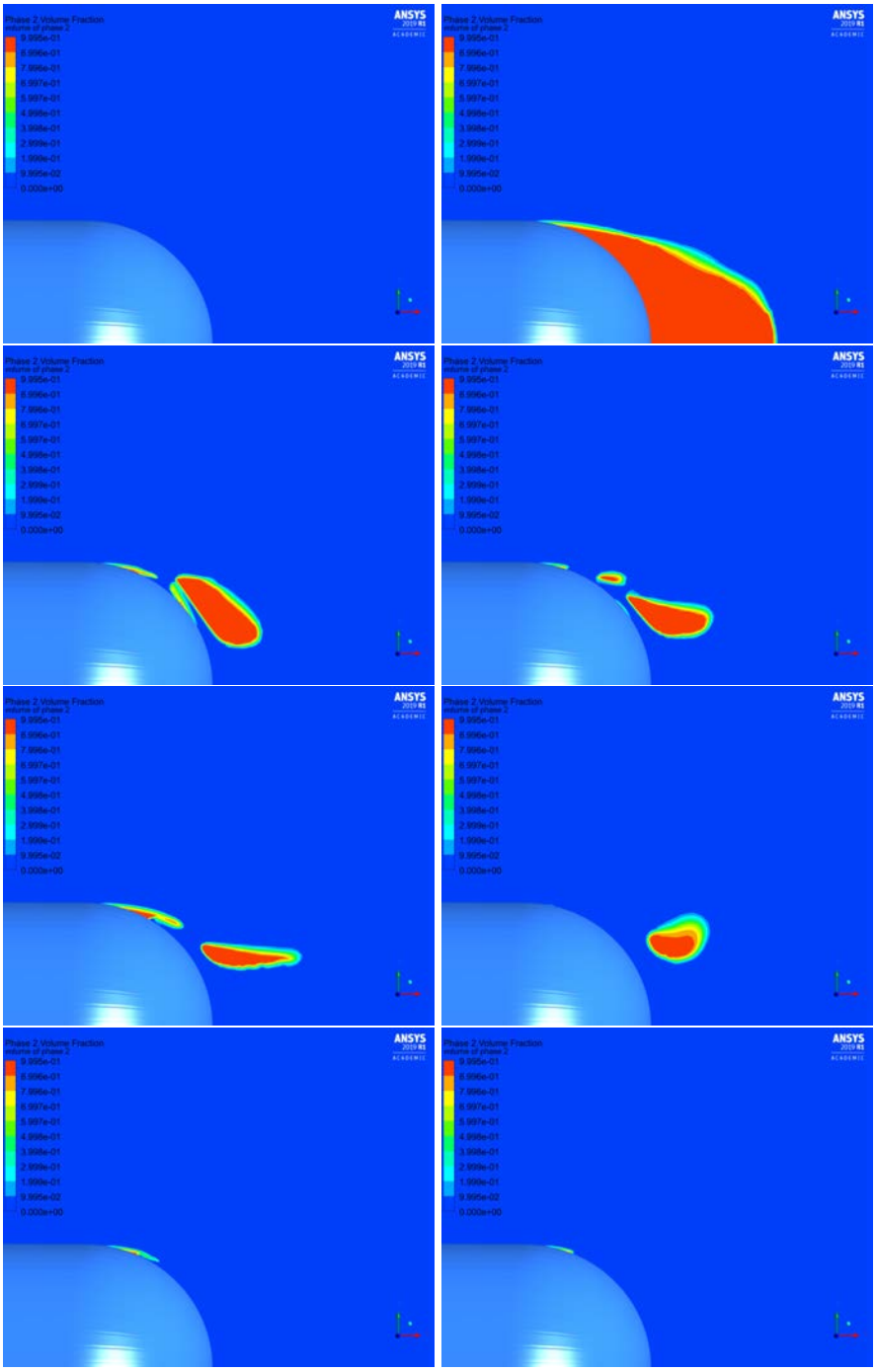

Figure 3.18: Vapour fraction contour in the wake at different time steps.

After the initial detachment, the fluid reattaches and maintains this behaviour.
What happens in the first seconds is a transition from a laminar boundary layer to a turbulent one. Indeed, the thickness of the boundary layer grows from about $0.3mm$ to about $5mm$ (figure 3.17).
Simulations show how long it takes: the collapse time of the wake bubble is about $1ms$ which coincides with the transition time from laminar to turbulent boundary layer.
In the figure 3.19 we can see the pressure that does not reach values such as to allow cavitation (figure 3.19). Some typical structures of the swirling cavitat-

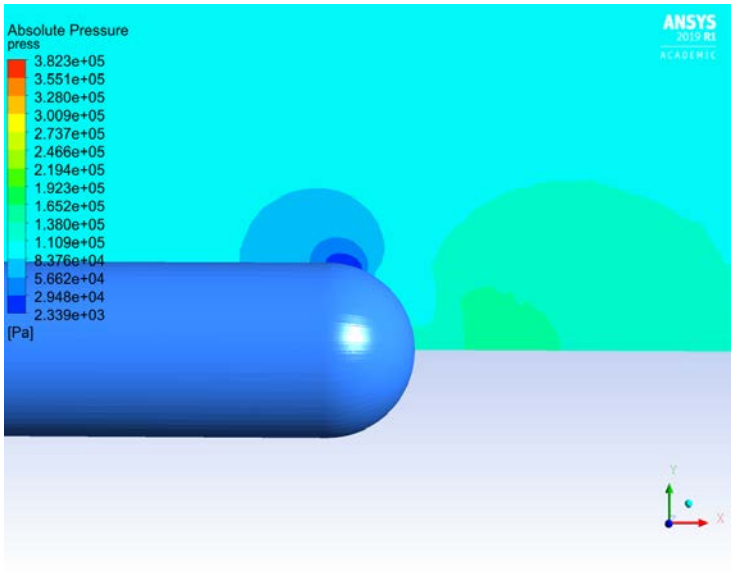

Figure 3.19: Absolute pressure distribution in the wake at $14ms$

ing wake are shown between $1ms$ and $10ms$ (figure 3.20): the near-wake and the transition zone. The model, instead, does not seem to predict the vortices of Von karman (probably a LES model is needed).
Despite this we see that simulations clearly show near wakes. These, following the formulations of Belahadji et al., have a well-defined period of oscillation whose

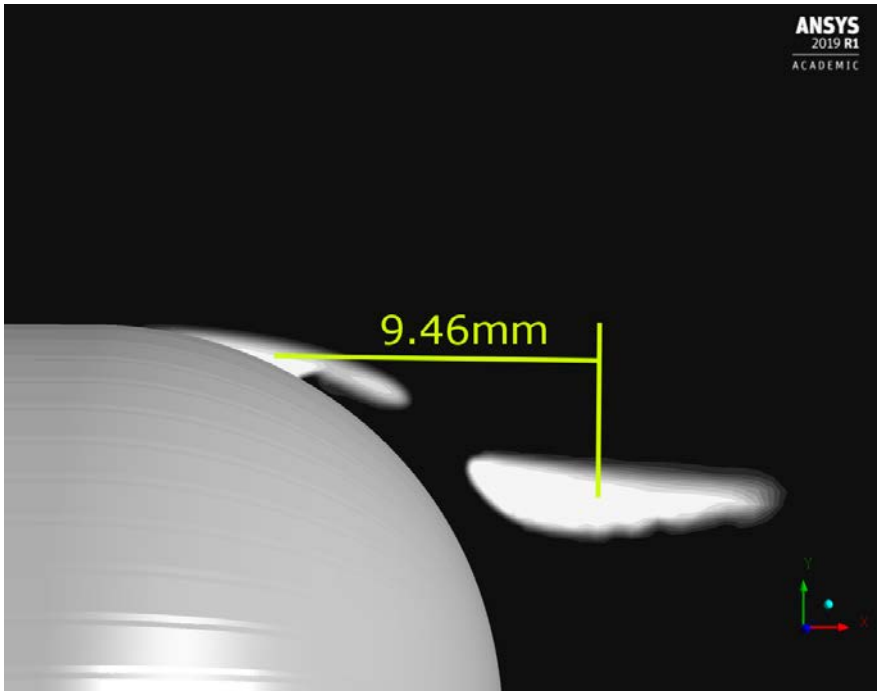

Figure 3.20: Near wake structures at 7ms.

wavelength λ is given by the formula:

$$\lambda_0 = \frac{\pi\delta}{\alpha} \tag{5}$$

where α is a dimensionless parameter that is considered equal to 0.38. The value of λ found with this theoretical formulation is $11.1mm$ in agreement with that found from simulations $9.46mm$, with a relative error of approximately 15%.
If the near wake zone is quite well predicted, the transition zone seems to appear in few moments, but there is not enough data to analyse it.

3.6.2 Cavity analysis

Simulations show that bubbles go through 3 phases:

- the formation;

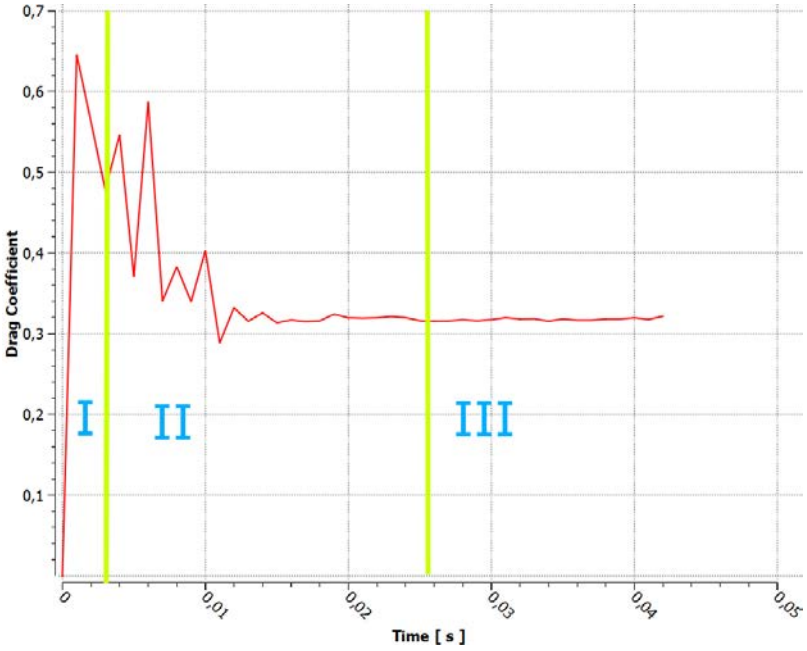

Figure 3.21: I: cavity formation; II: cloud cavitation zone; III: stable cavity.

- a pseudo periodic phase: cloud cavitation;
- stable cavity.

In order to demonstrate this, the drag coefficient was plotted over a period of $0.5s$(figure 3.21).

The first phase of cavitation is well defined while the last two do not seem so, for this reason, the c_d graph is purely indicative. It shows that bubble cavitation occurs when the drag coefficient fluctuates with large amplitude while a stable cavity appears at the end of the simulated time.

Bubble Formation. The complete formation takes place between 2ms and 3ms. First of all the boundary layer detaches, according to the law:

$$s_{LS,C} - s_{LS,NC} = -2.37[\frac{1+\sigma}{Cp_{LS,NC}}][s_{LS,NC} - s_{Cp_{min,NC}}] \tag{6}$$

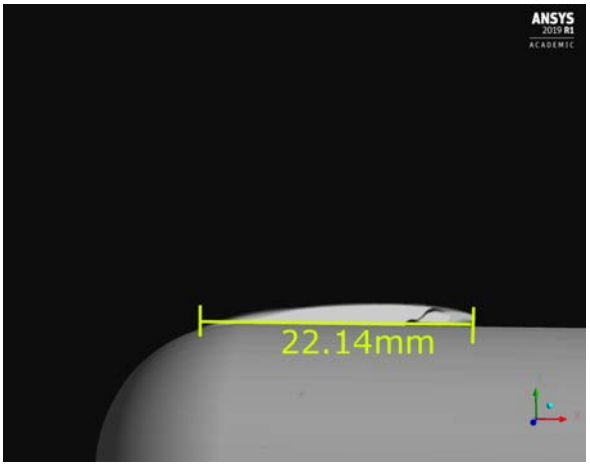

Figure 3.22: Cavity length at 3ms.

From our model this difference turns out to be in accordance with the predicted one.

The length of the cavity instead is $L = 22.4mm$ with a diameter $D = 28.9mm$.

No experimental data was found on the bubble, but a visual comparison with the photographs of Rouse and Mcnown can give an idea of the goodness of the simulation (figure 3.23).

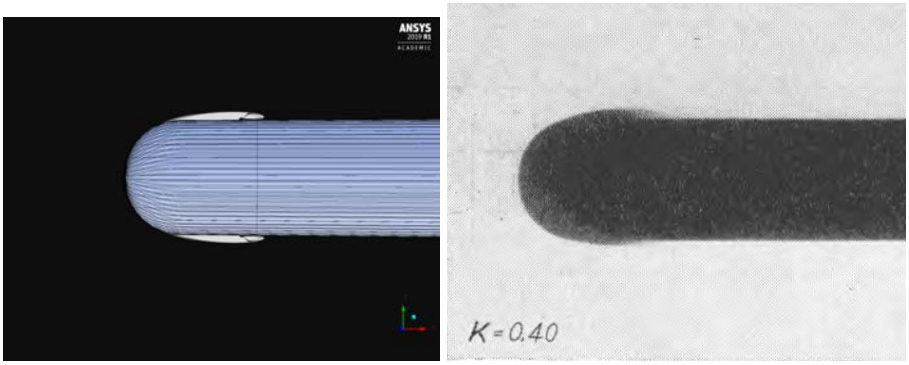

Figure 3.23: Graphical comparison between cfd model (left) and experimental model (rigth)

Cloud Cavitation. It is evident how partial cavitation can occur in different patterns [1], and the boundaries between them are not well defined.

Although this scheme (figure 3.24) is defined for an aerodynamic profile, the structures found in the simulation appear in line with those presented [1].

In particular, for $\sigma_c = 0.4$, the zone in which the flow develops is the one highlighted in green (figure 3.24).

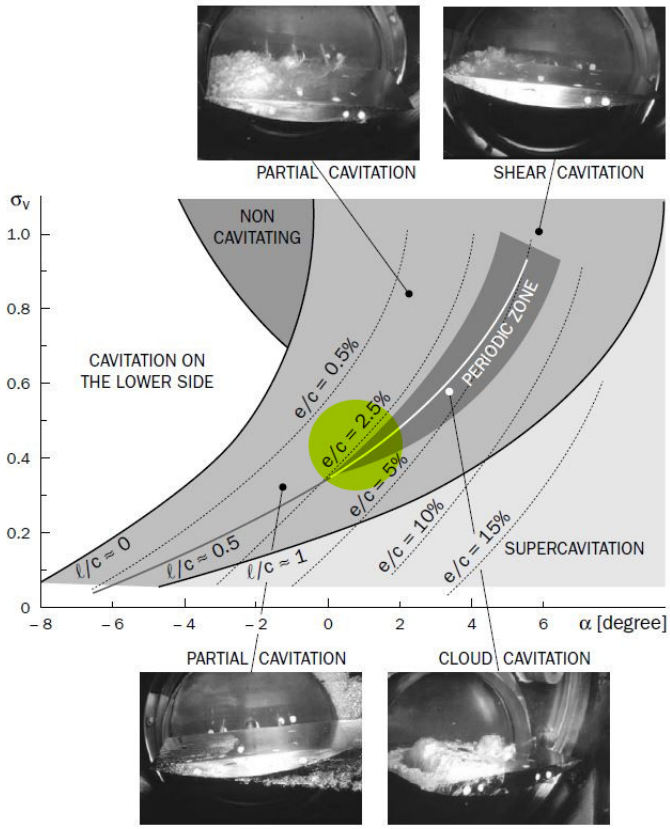

Figure 3.24: Main cavity patterns for a hydrofoil at $Re = 2E + 06$

In this chapter we want to define a way to recognize the periodical behaviour of bubble cavitation.

We have proceeded in two ways (figure 3.25):

- plots the volume of vapor, trying to recognize periodic trends;

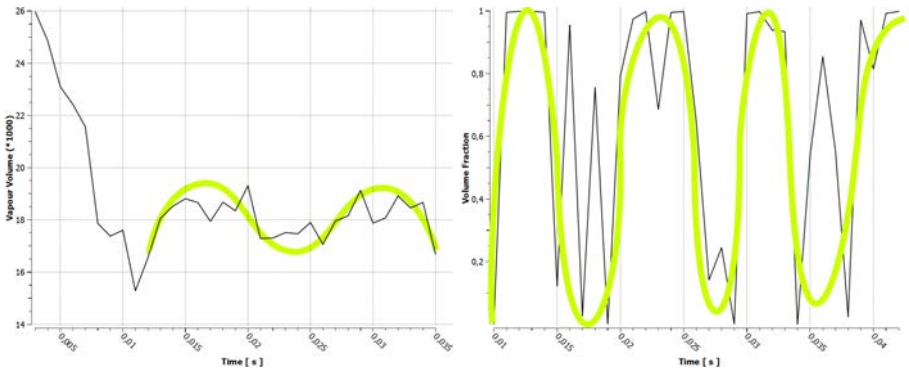

Figure 3.25: On the left: Average vapour volume - Time; on the right: Volume Fraction computed in a point near the wall.

- studying certain visually determined points where the cavitation bubble tends to collapse.

Results show periodic fluctuations in the average amount of vapor both in the volume and in the considered point.

Although the results encourage further study, for the purposes of the thesis analysing quantitatively these data does not provide interesting insights for the final goal.

Nevertheless, it is very interesting that these fluctuations always tend to have a period of about 1ms. This characteristic time is common to all phenomena that appear in the evolution of the fluid.

This results to be partially in disagreement with the theory, which previews T=1.64ms.

The model also shows one of the fundamental aspects of cavitation: the re-entrant jet.

Without getting lost in theoretical aspects previously addressed, it is evident that simulations are able to effectively predict the behaviour of the fluid, showing the liquid re-entrant jet.

As foreseen by the theory, its thickness covers 30% of the cavitation bubble, and has a velocity equal to about V_∞ ($V_\infty(1+\sigma)$).

Moreover the goodness of simulations is evidenced by the fact that resuming the

diagram of the pressures, the overpressure at the end of the cavity is determined from the collapse of the bubbles of cavitation (cloud cavitation).

It is verifiable that an increase in the fluid stability translates in a decrease of this overshoot.

The jet is the cause of the bubbles collapse, the bubbles collapse causes the overpressure and the overpressure causes the jet formation (figure 3.26,3.28,3.29).

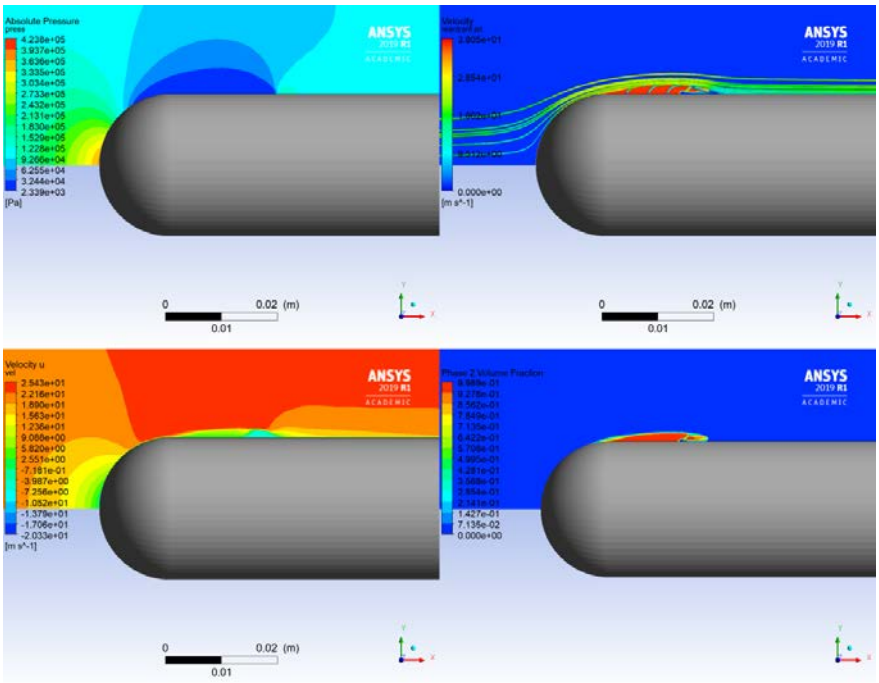

Figure 3.26: Pressure, Streamline, U Velocity and Volume Fraction for cloud cavitation with jet formation at 3ms

Stable Cavity (Partial Cavitation). Although there are these periodic phenomena, dividing cloud cavitation and stable cavitation is purely theoretical.

In both phases there is a reattachment and detachment of the fluid, also evidenced by the graph of pressures that shows that pressure coefficient on the wall is not 0.4 and it tends to grow at the end of the cavity.

Two interpretations have been given to the model:

- bubble cavitation and partially cavitation are two different interpretations of the same thing (mixed phase);
- the two behaviours are defined by the greatness of the single bubble. When it is denser and longer we can consider the cavity more stable.

We choose to interpret the two behaviours as distinct.
The elements that distinguish the phases are respectively two: the thickness of the jet and the distance between the broken bubbles by the jet.

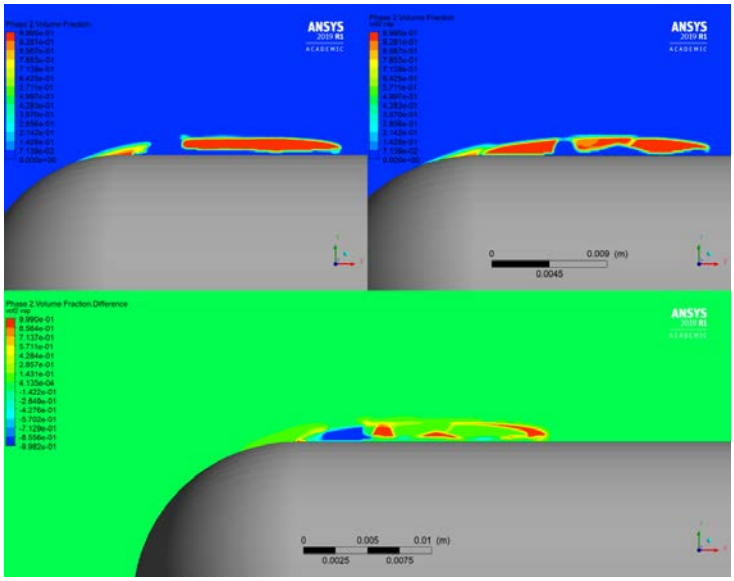

Figure 3.27: Bubble patterns at different time steps.

In figure 3.27, we see that the right bubble turns out to be undivided, even if there are some spots in which there is very little mass of vapor. On the other hand, the left image shows a bubble that is completely detached from the wall and a new cavity is growing. We do not know if this behaviour fails to meet physical reality because we do not find sufficient researches, but we have try to find an answer in order to inspire new studies.

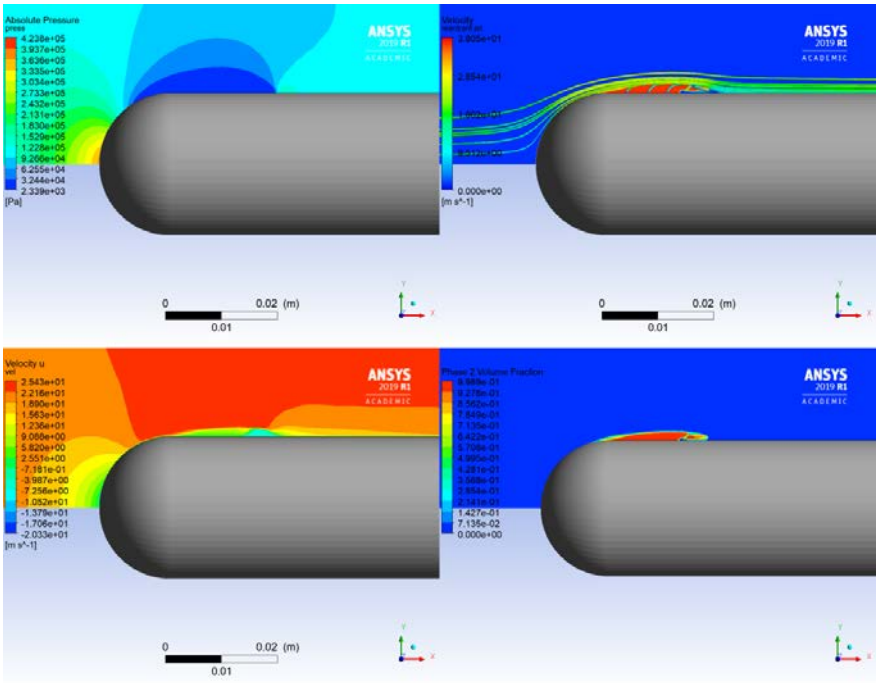

Figure 3.28: Pressure, Streamline, U Velocity and Volume Fraction for cloud cavitation with jet formation at 6ms

3.7 Conclusion

The model is validated both in qualitative and quantitative terms, as regards the parameters which we are most interested in, such as pressure and drag coefficients.

The next chapters deal with these last two, that assume a predominant importance in order to achieve the objectives set.

As far as the more intimate nature of the fluid is concerned, the results have been considered as a good approximation, despite some problems were found interpreting the time evolution.

The main issues were:

- finding good data to compare our results;
- using k-ϵ models that give good results for c_D and c_p does not ensure good

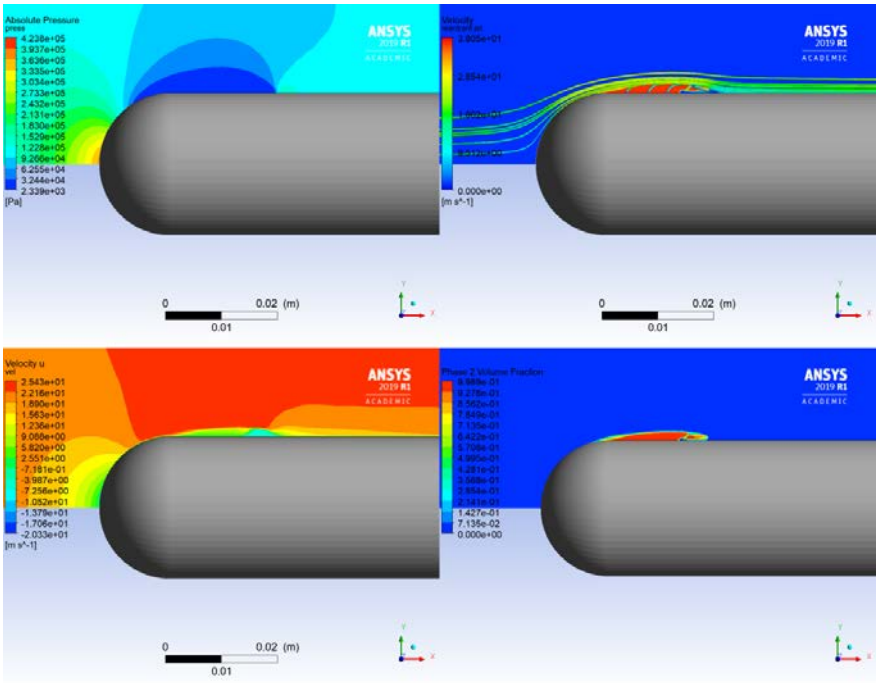

Figure 3.29: Pressure, Streamline, U Velocity and Volume Fraction for cloud cavitation with jet formation at 9ms

results in temporal behaviour. Indeed, these data are highly sensitive to turbulence model choice [15]. Clearly a LES (large-eddy-simulation) would give better results.

Finally, Further researches will be conducted in order to solve these issues, aiming to validate models that describe better the cavitation patterns. We suggest to study hydrofoils for which can be found a much broader literature.

4 3D Validation

3D simulations were run in order to have tools to study cavitation three-dimensionally and for further studies that deal with ventilated cavity.

4.1 Geometry and Mesh

The studied geometry was a 22.5 revolution of the 2D geometry investigated in the previous chapter. The aim was to reduce computational costs and to guarantee the opportunity to insert a ventilation system without influencing the simulations goodness.

The diameter of the domain has been 127mm and not 254mm because this preliminary study did not seem to require too wide domains.

As far as the mesh is concerned, a polyhex mesh (749624 nodes) was chosen to reduce convergence instability, combining an inflation layer that simulated the boundary layer in the proximity of surfaces.

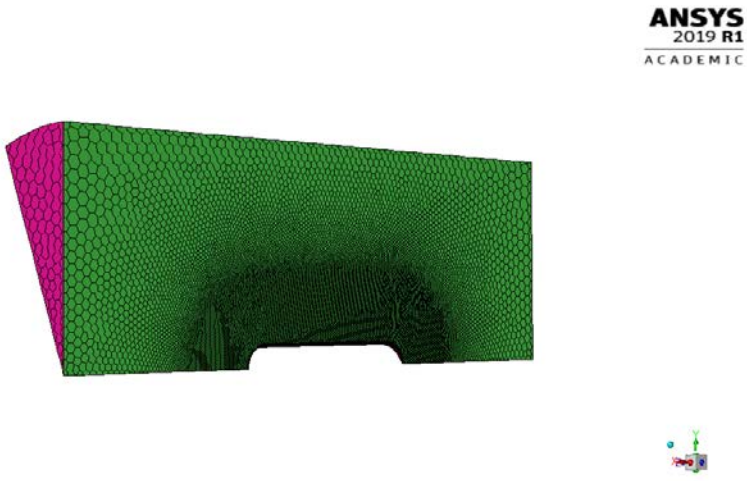

Figure 4.1: Polyhex 3D mesh.

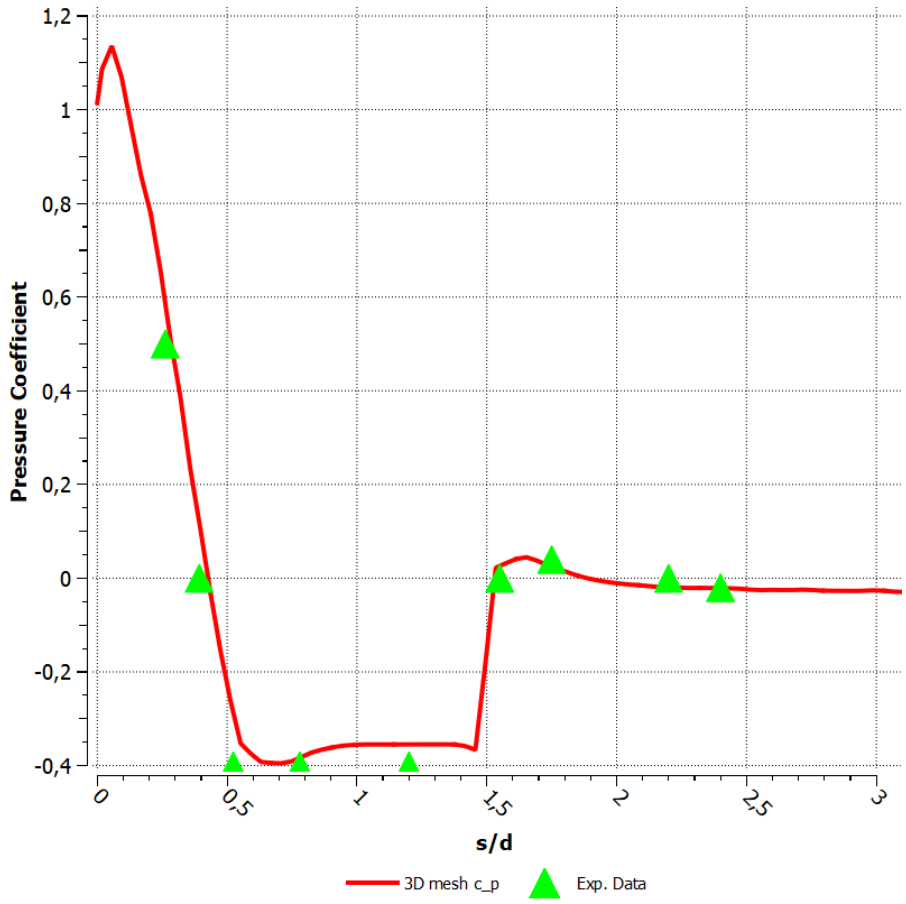

Figure 4.2: 3D mesh c_p distribution.

4.2 Results

Setups used for 3D simulations were the same used for 2Ds, only differencing in the boundary conditions: on the mesh side faces was introduced symmetry condition, which we will replaced with the periodicity condition in upcoming studies.

Results were averaged as always over 14ms and they showed their goodness, even compared to 2D sizing.

Besides, some of them seemed to encourage the use of 3D meshes (figure 4.2):

- pressure coefficient on geometry tip was equal to 1, respecting more pre-

cisely physics, despite the use of a k-epsilon model;

- a similar approach could be taken to the pressure overshoot, which was more similar to the curves drawn by Rouse and Mcnown [5]. However, we reserved the right not to take a definitive position on this because discordant opinions have been found on this issue[1, 5, 9, 7, 2].

In conclusion, a further possible development of the thesis is to study the 3D behaviour of the fluid, introducing the concept of the periodic boundary conditions.

5 Shape Comparison and Supercavitation

In the previous chapter the model was validated.
Now, experimentation has turned to test different conditions for different geometries:

- a hemispherical head geometry;
- a flat head geometry;
- a cone head geometry.

The objective is studying drag in different operating conditions:

- partial cavitation at high sigma
- supercavitation at low sigma.

A new geometry will be studied with the obtained information, in order to have low drag at high sigma, a supercavitation profile at the lowest possible speed and the opportunity to implement a ventilated cavitation.
Partial cavitation was studied focusing on the following conditions:

- inlet velocity of 22.15 m/s;
- inlet velocity of 25.71 m/s.

while for supercavitation:

- inlet velocity of 40.55 m/s;
- inlet velocity of 49.64 m/s;
- inlet velocity of 70.41 m/s.

Aiming to design a final model, we introduce some relevant results.

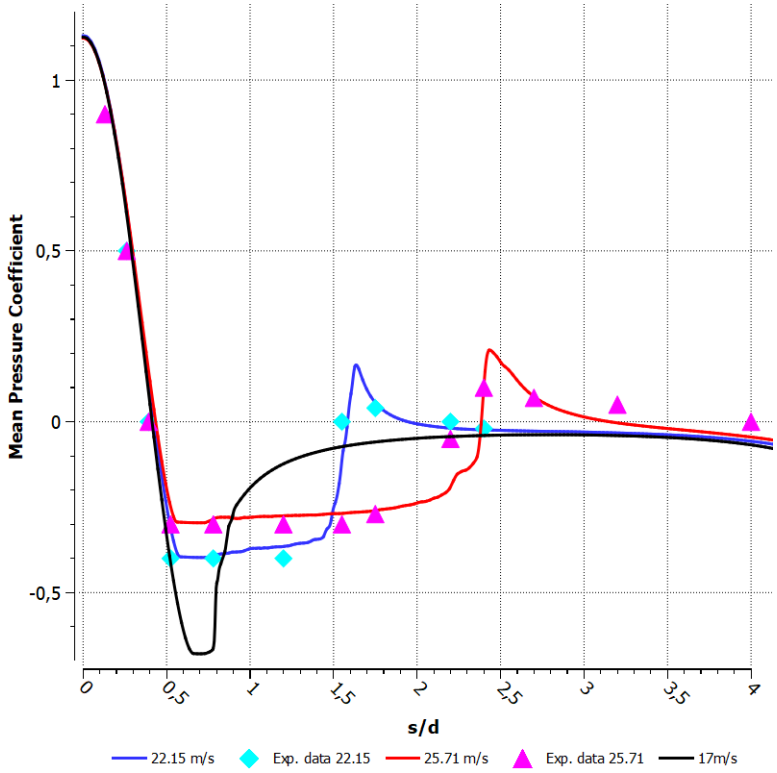

Figure 5.1: c_p distribution at 22.15m/s, 25.71m/s and 17m/s. 22.15m/s corresponds to $\sigma_c = 0.4$, while 25.71m/s corresponds to $\sigma_c = 0.3$ and they were both validated. No experimental data was found for the speed of 17m/s ($\sigma_c = 0.68$.

5.1 Partial Cavitation

We continued first to study hemispherical head, adding a 30 knots simulation to understand what happens at ”very low” speeds.

Plotting the pressure coefficients, we had the opportunity to figure out pressure variations around the profile.

Furthermore, from the graph below (figure 5.2), we learned that the drag coefficient increases from 0.24 to 0.36 as speed increases and cavitation number decreases. Drag consists of pressure drag and viscous drag.

While pressure drag rises from 0.15 to 0.32 increasing velocity, viscous drag has an opposite behaviour. Indeed, it drops by 58% from 30 knots to about 40 knots,

decreasing with speeds. We analysed it in percentage terms because the larger a vehicle is, the bigger advantages it has (figure 5.3). This is due to the fact that the vapor cavity covers a part of geometry.

We studied this new formulation:

$$c_{v_0}\% = \alpha_e(\sigma_{30kn} - \sigma) \tag{7}$$

where α_e depends on body shape. We also created a graph, only valid for speeds lower than 42 knots.

Using hemispherical head with high sigma results in an increase in drag due to stagnation on tip. For this reason, other geometries as the cone has been preferred in the past.

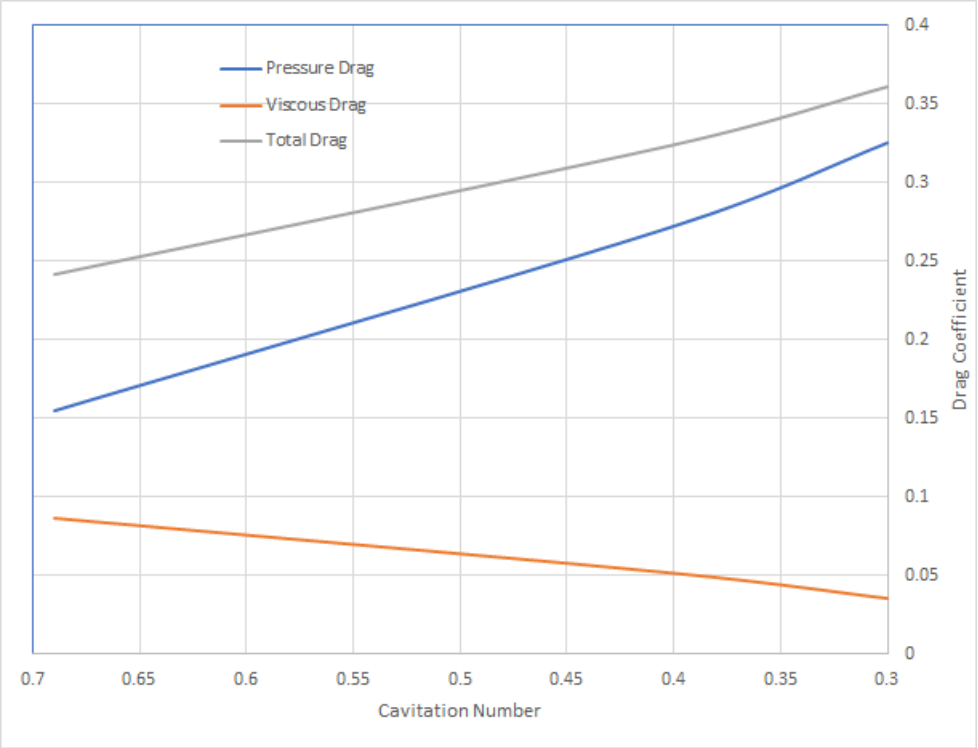

Figure 5.2: Drag coefficient and its components varying speed

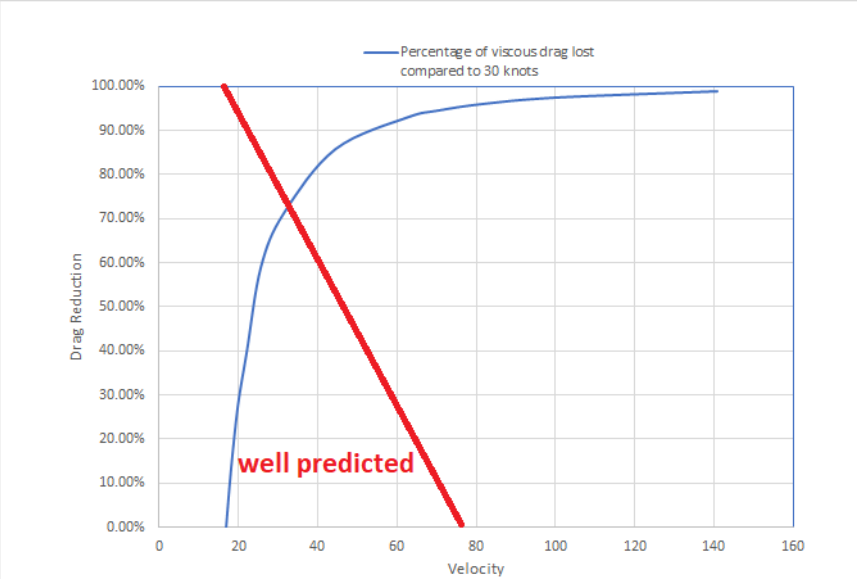

Figure 5.3: c_v reduction due to cavitation number decreasing; the red line defines the well predicted zone.

The incipient point of cavitation is at s/d=0.56.

This point has a key role indeed, the sooner the separation happens the sooner there will be a pressure reduction on profile tip, lowering drag.

This leads to an initial evaluation:

- detaching fluid as soon as possible allows to reduce pressure drag;
- increasing the cavitation bubble as much as possible allows to reduce viscous drag.

In order to achieve these results, some geometries with very different behaviour have been identified following researches done in the bibliography of the thesis [2, 5, 7, 9] (figure 5.4).

The cone head (table 1) has a very low drag at low sigma, but the cavitation bubble is minimally developed.

An ogive head takes to extremes these specifications: cavitation starts to have

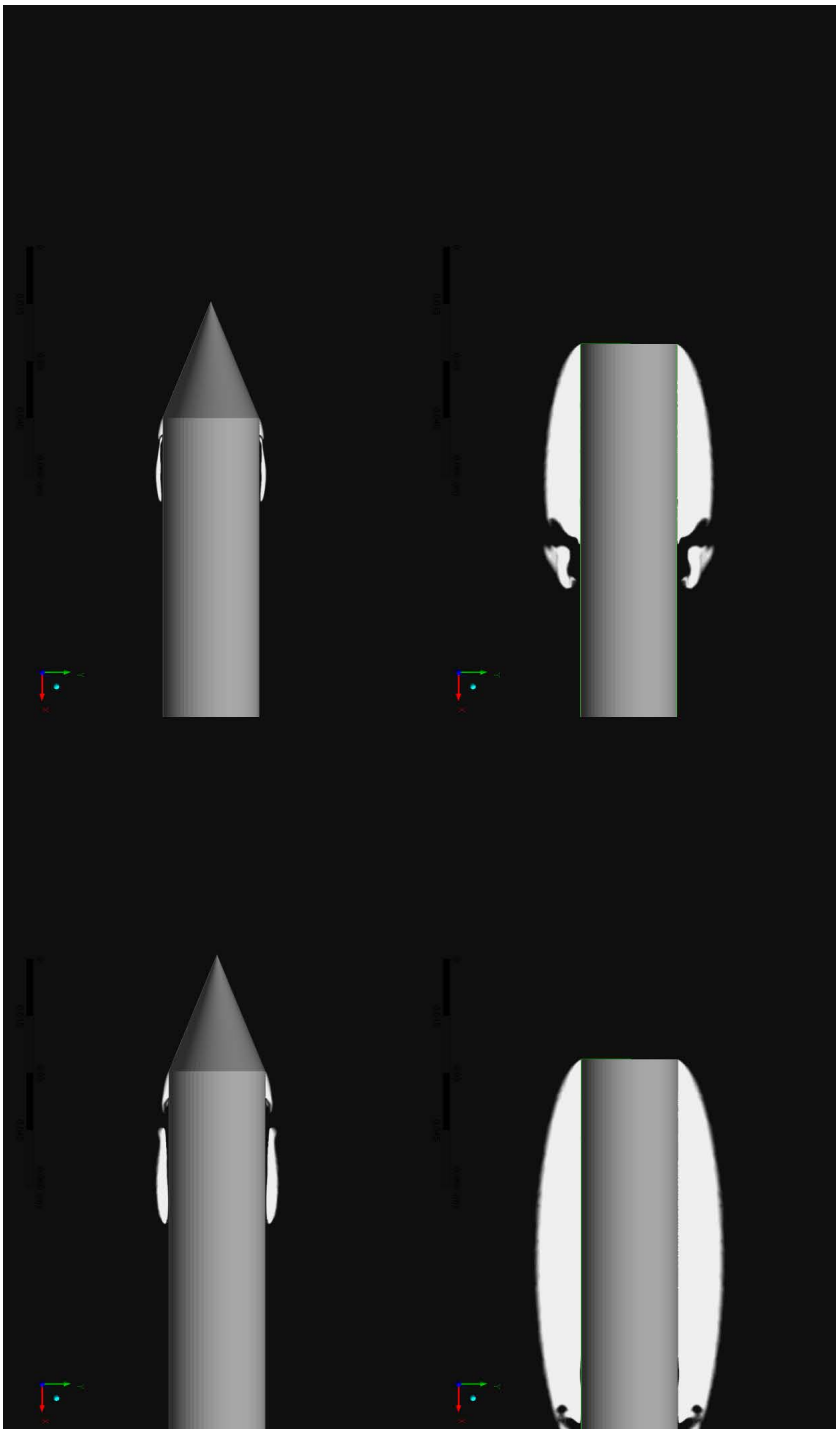

Figure 5.4: New profiles tested.

appreciable dimensions at about 30 m/s (55.53 knots) that's why it will be used to design engine inlets.

This kind of geometries are perfect for low speeds, but they can be improved for higher.

This is the reason why supercavitation has been developed.

Speed	Drag Coefficient	Bubble Length (s/d)
22.15 m/s	0.341	0.85
25.71 m/s	0.369	1.56

Table 1: Bubble length and pressure coefficients for different speeds. (Cone Cavitator)

On the other side there are flat heads (table2).

Their behaviour is exactly the opposite of cone heads.

First of all, the maximum cavitation length is really remarkable, even at high sigma. The cavity length is about 4D (4 times the diameter) at 25.71 m/s (about 40 knots).

Results are therefore encouraging as regards the bubble length, but they are not so encouraging for drag.

Speed	Drag Coefficient	Bubble Length (s/d)
22.15 m/s	0.7064	2.519
25.71 m/s	0.721	3.95

Table 2: Bubble length and pressure coefficients for different speed. (Flat Head Cavitator)

Nevertheless, the viscous drag is much lower than the other heads.

In table 3 is presented a comparison between investigated geometries at different speeds and the hemi-head at 30knots in terms of percentage.

Concluding:

- from figure 5.6, it is evident that conical heads generally have lower pressures; however the zero crossing point shifts by about s/d=1.25. Besides,

Geometry	Cavitation Number	Viscous Drag Reduction(hemi 30kn)
Hemi	0.3	40%
Hemi	0.4	58%
Cone	0.3	42%
Cone	0.4	55%
Flat	0.3	97%
Flat	0.4	96%

Table 3: Geometry/Cavitation number - viscous drag reduction

generating small bubbles implies high drag due to the viscous forces with very long vehicles;

- flat heads have long cavity even at low speeds, but very high drag coefficients;
- cavitation appears always in geometry discontinuities.
- analysing pressure contours, we understand that inside the bubble there is

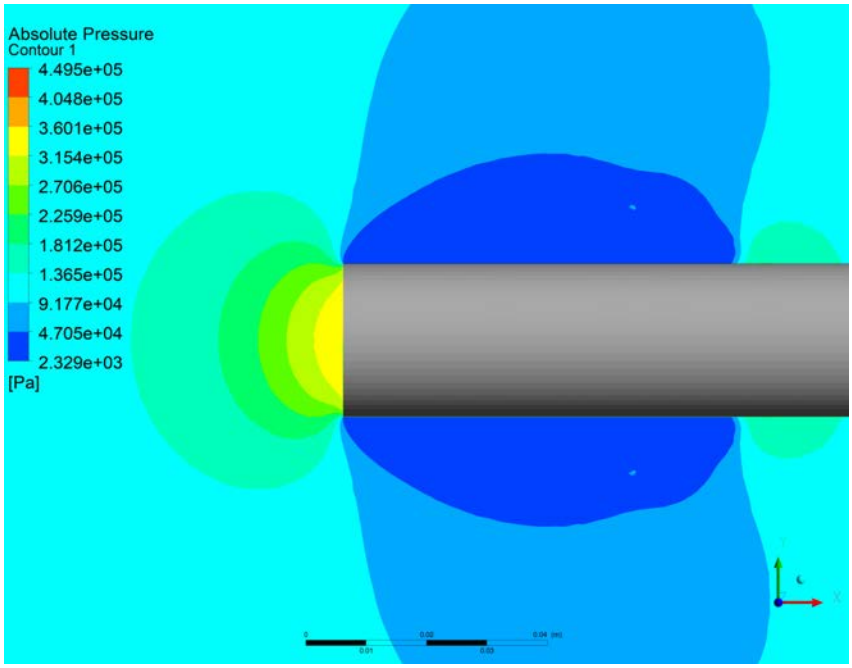

Figure 5.5: Pressure contours for flat head.

a pressure drop. Triggering cavitation is an easy way to reduce drag due to appendices, because we can envelop them with a vapor cavity; further developments will be investigated in next sections.

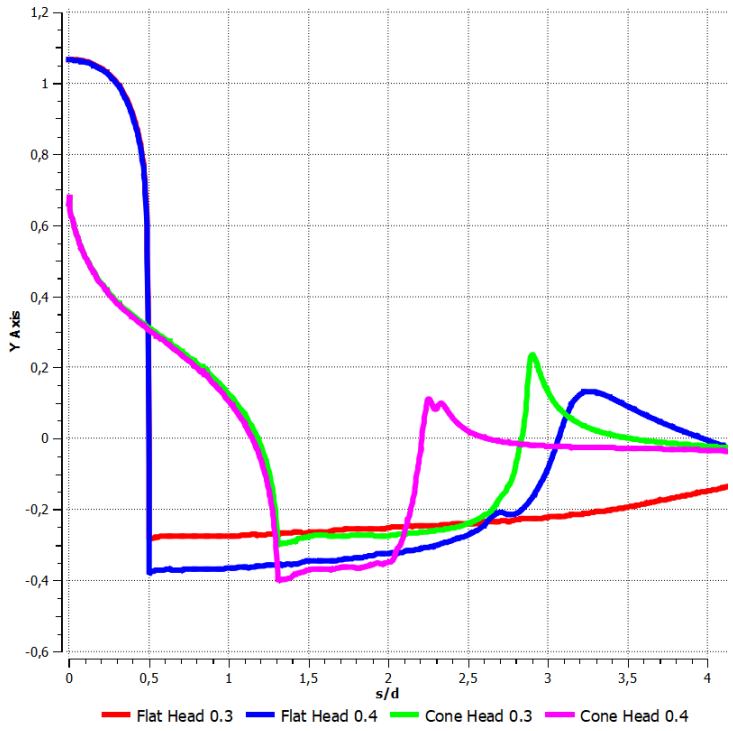

Figure 5.6: c_p distribution around cone cavitator and flat head cavitator at differente velocity conditions.

5.2 Supercavitation

First analysis focused on cavitation inception. We also discovered pros and cons of each geometry. We are now moving to supercavitation that we will define as our *fully operational condition*.
It is possible to define this law [1, 2]:

$$c_x = (1 + \sigma)c_{x_0} \tag{8}$$

Even if a previous validation has been performed, we proceed to validate a new mesh through Yang et al. data [2] keeping unchanged the conditions set for partial cavitation.

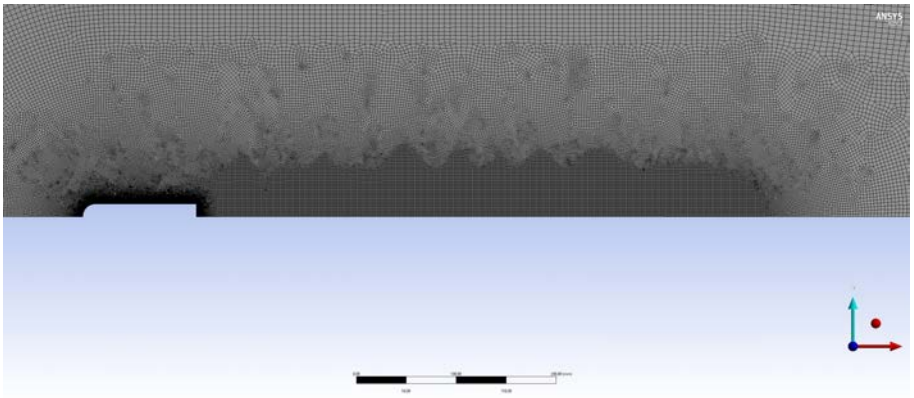

Figure 5.7: New mesh for supercavitating geometries.

Modifications are carried out taking into account two factors:

- increasing in cavity length caused by higher speeds led to insert refinement as large as the predicted bubble;
- increasing in perturbations, forces to increase the domain behind the body of 100d.

The Reichard formulae [1] were used to choose the length of the refinement.
These show that ratio between cavity length is independent from bubble diameter, allowing to compute an expected length in order to define the refinement:

$$\sigma = 0.6856$$
$$l/d_m = \frac{\sigma + 0.008}{\sigma(0.66 + 1.7\sigma)}$$
$$c_d = 0.82(1 + \sigma)$$
$$d_m/d = (\frac{c_d}{\sigma - 0.132\sigma^{(8/7)}})^{0.5}$$

With these equations, we calculated a refinement length of 650mm , expecting good predictions on results in terms of pressure and drag.
The same equations were used for the diameter which is 35mm.
The shape of the cavity is elliptical, that is why an ellipse was chosen like BOI (body of influence).

5.2.1 Shape Comparison

Again we study bubble length and c_d.
Analysing hemispherical heads, we recognize a very similar behaviour to partial cavitation, previously seen.
Cavities always maintain a spherical geometry and tend to evolve exponentially in length.
Indeed, they become seven times larger varying speed of about 30m/s. The diameter grows almost linearly.
The point of detachment is almost the same of partial cavitation (s/d=0.56).
As far as cone head is concerned, results show a very particular behaviour.
The cavity tends to develop in its diameter rather than on its length and this is in disagreement with theoretical predictions.

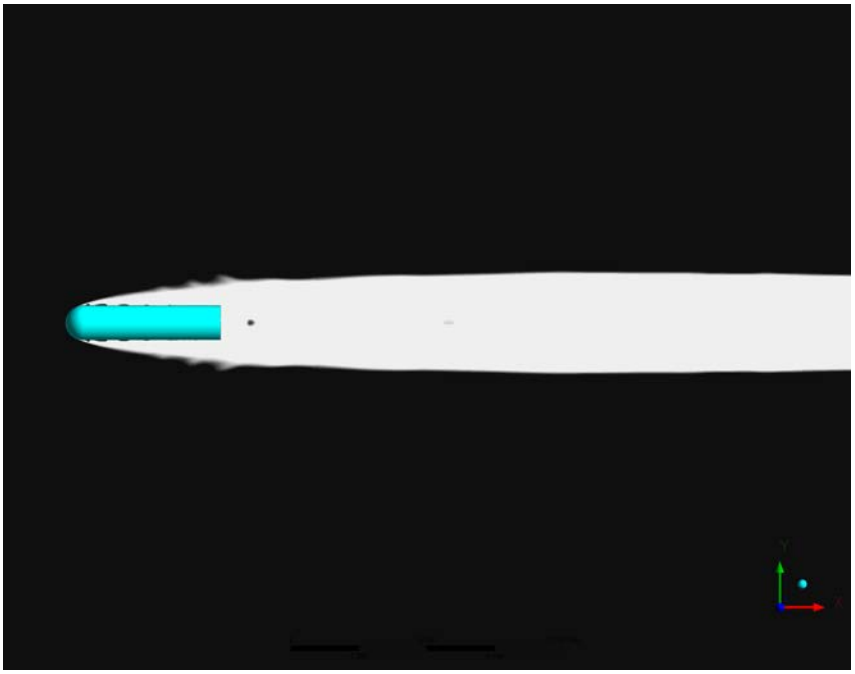

Figure 5.8: Cavity at 70.41m/s (σ_c = 0.04)

The theories, despite this, are mainly studied on flat heads so may be an explanation to this contradiction.

The ratio between length and diameter is always increasing with speed. Furthermore, this value approaches an asymptote when σ_c approaches 0.

For practical reasons, it is clear that a bubble of this size, however stable it may be, can only be used for blunt bodies.

Fast fluid reattachment involves an increase in viscous drag and overpressure, causing further increases.

For these reasons conical heads will not use to have better performances.

Bubble length of flat heads is absolutely amazing in supercavitating conditions.

It behaves very similarly to the round head but cavity lengths demonstrate why they have been used over the years on Russian torpedoes.

At speeds between 30 and 50 m/s (100-180 km/h), cavities are twice as long as

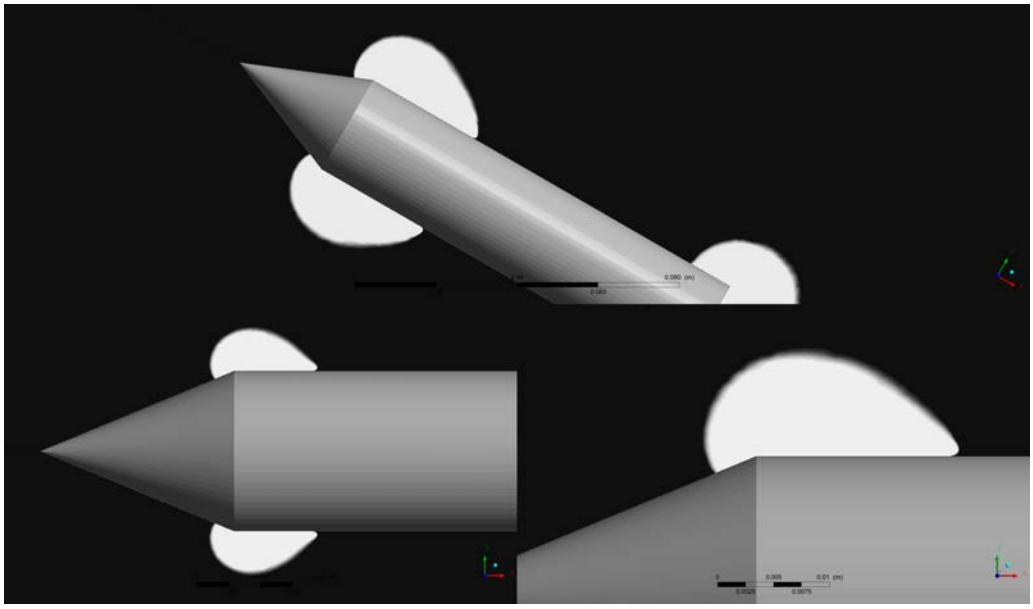

Figure 5.9: Cone cavitator at different speed. Top: V_∞ = 70.41; Bottom-Left: V_∞ = 49.64; Bottom-Right: V_∞ = 40.55

the hemispheric heads.

At higher speeds (70m/s) they reach 44 times their diameter.

A further consideration can be made: following analyses it seemed that at speeds between 40-55m/s the bubble still has some instability.

In particular, conical and rounded series show detachments along their bodies, unlike flat heads.

This is a big point to pay attention to.

These instabilities are not significant in a simulation environment but they can trigger abrupt changes with consequences as erosion and rapid drag growths.

The conclusion, however obvious, is to prefer flat heads both for the predictability of results and for cavities stability.

Bubble length and bubble diameter could be seen in the table below:

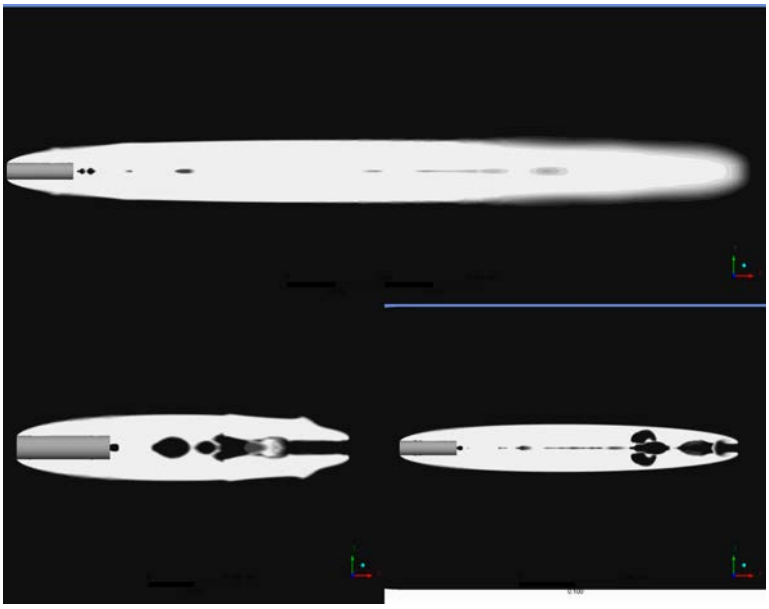

Figure 5.10: Flat head cavitator at different speed. Top: $V_\infty = 70.41$; Bottom-Left: $V_\infty = 49.64$; Bottom-Right: $V_\infty = 40.55$

Speed	l_{cavity}/d	d_{cavity}/d
70.41m/s	33.26	1.52
49.64m/s	10.23	0.94
40.55m/s	7.02	0.87

Table 4: Hemisphere Cavitator

Speed	l_{cavity}/d	d_{cavity}/d
70.41m/s	1.36	2.16
49.64m/s	0.87	1.71
40.55m/s	0.65	1.51

Table 5: Cone Cavitator

Speed	l_{cavity}/d	d_{cavity}/d
70.41m/s	43.86	1.85
49.64m/s	23.85	1.66
40.55m/s	14.26	1.42

Table 6: Flat Head Cavitator

5.2.2 Drag Coefficient Comparison

Studying c_d found through cfd analysis has a double meaning:

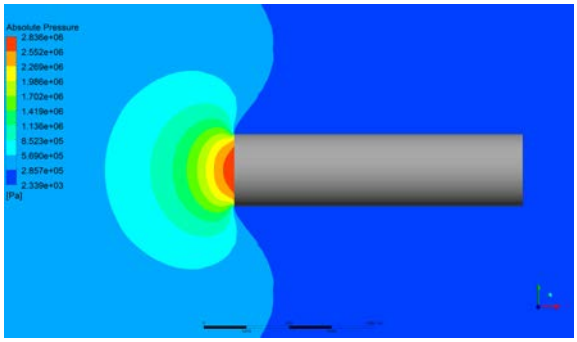

Figure 5.11: Pressure Distribution at $V_\infty = 70.41 m/s$

- first of all, to definitively find out if model describes the phenomenon precisely through both theoretical [1] and experimental tests [2].
- secondly, to analyse critically how we can proceed to reduce drag in supercavitation phase.

Again we use Reichardt formulas.

The experimental c_{x0} [1] is equal to 0.340 [2] for a spherical head while cfd analyses give cd of 0.359 with a relative error of 5.6%. We consider it a good result.

Moreover, we compare all the values obtained using the formula

$$c_x = (1 + \sigma)c_{x0}$$

and we display results in the following table (7).

Geom/Speed	c_d theoretically predicted	c_d computed	error
Hemi/49.64m/s	0.38	0.37	2.8%
Hemi/40.55m/s	0.40	0.39	2.08%
Cone/49.64m/s	0.236	0.248	4.79%
Cone/40.55m/s	0.245	0.287	16.94%
Flat-head/49.64m/s	1.02	0.99	3.21%
Flat-head/40.55m/s	1.06	1.012	4.60%

Table 7: Cavitators comparison.

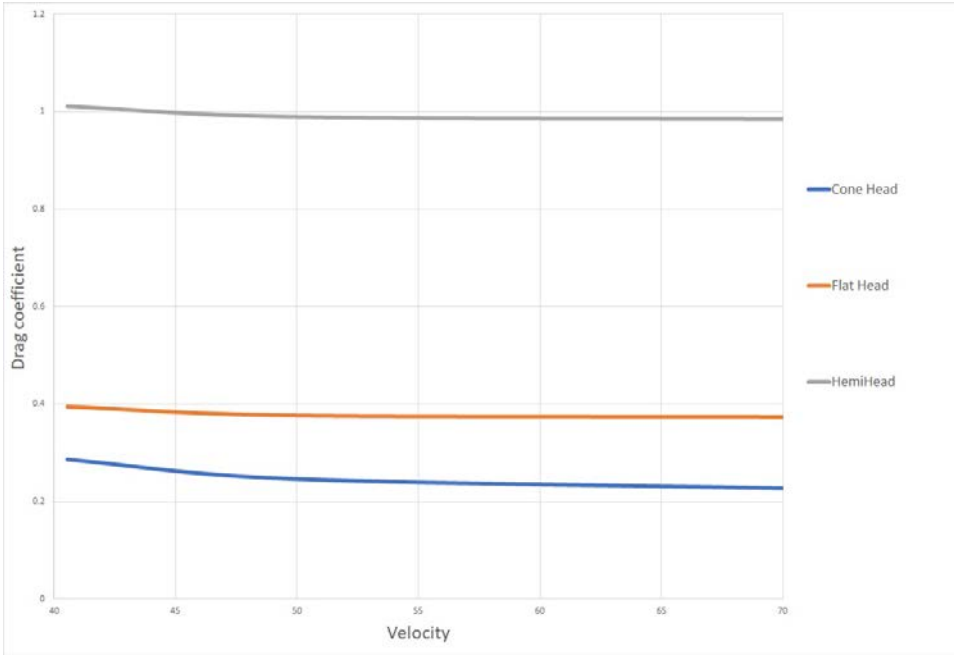

Figure 5.12: c_d comparison between the three geometries.

The model reproduces results very precisely.

They show that conical heads have smallest drag. In addition, the graph below (figure 5.12) shows that although the viscous drag is completely eliminated by flat heads, there is a very big difference between the two curves (flat heads, hemispherical heads), which may discourage using a geometry to enhance supercavitation.

Finally, looking at pressure contours (figure 5.11), it is clear that the vapour pressure creates a low pressures boundary that we can exploit. Decreasing density causes a drag drop.

At this point, last geometries are tested in order to bring the drag coefficient below 0.2.

6 Supercavitating Geometry

Once the main aspects of the various geometries are identified, the goal is to create a new body that can drastically reduce drag.

This last simulation started from a rather simple concept that is linked to the very essence of the propulsion.

Leaving aside all the aspects closely related to the propulsion system, by definition drag will tend to grow as the speed increases.

It is sufficient to consider that, assuming a speed of 20m/s and a c_d of 0.3, the product $v^2 \times c_d$ equals about 120. For the same hypothetical body at a speed of $70 m/s$ and with an equal c_d, the value is 1470, about 12 times as much.

Usually the maximum thrust delivered by a propeller equals the maximum expected drag.

It was therefore essential to start from the maximum expected speed of 70.41 m/s and create a body that could lower the c_d compared to the best performance of the cone cavitator.

Then, starting from a c_d of 0.22 for the cone head, we aim to lower it below 0.20.

So studying the various models tried in history was tested a first geometry with a step on the tip [2](figure 6.1).

This combines the ability to generate large bubbles, typical of flat heads, along with the reduced drag of cone heads.

The first test with a 6 mm step was discouraging because the drag coefficient was 0.235. Moreover, the bubble did not cover the whole head and the overpressure due to the re-entrant jet increased the drag on the head.

But after that, a 5mm step head was tested.

Results were about what one would expect: c_d was widely below the threshold, demonstrating the goodness of all our considerations. The drag coefficient was 0.16 with a consequent 29.79% reduction in drag. All this is due to the fact that

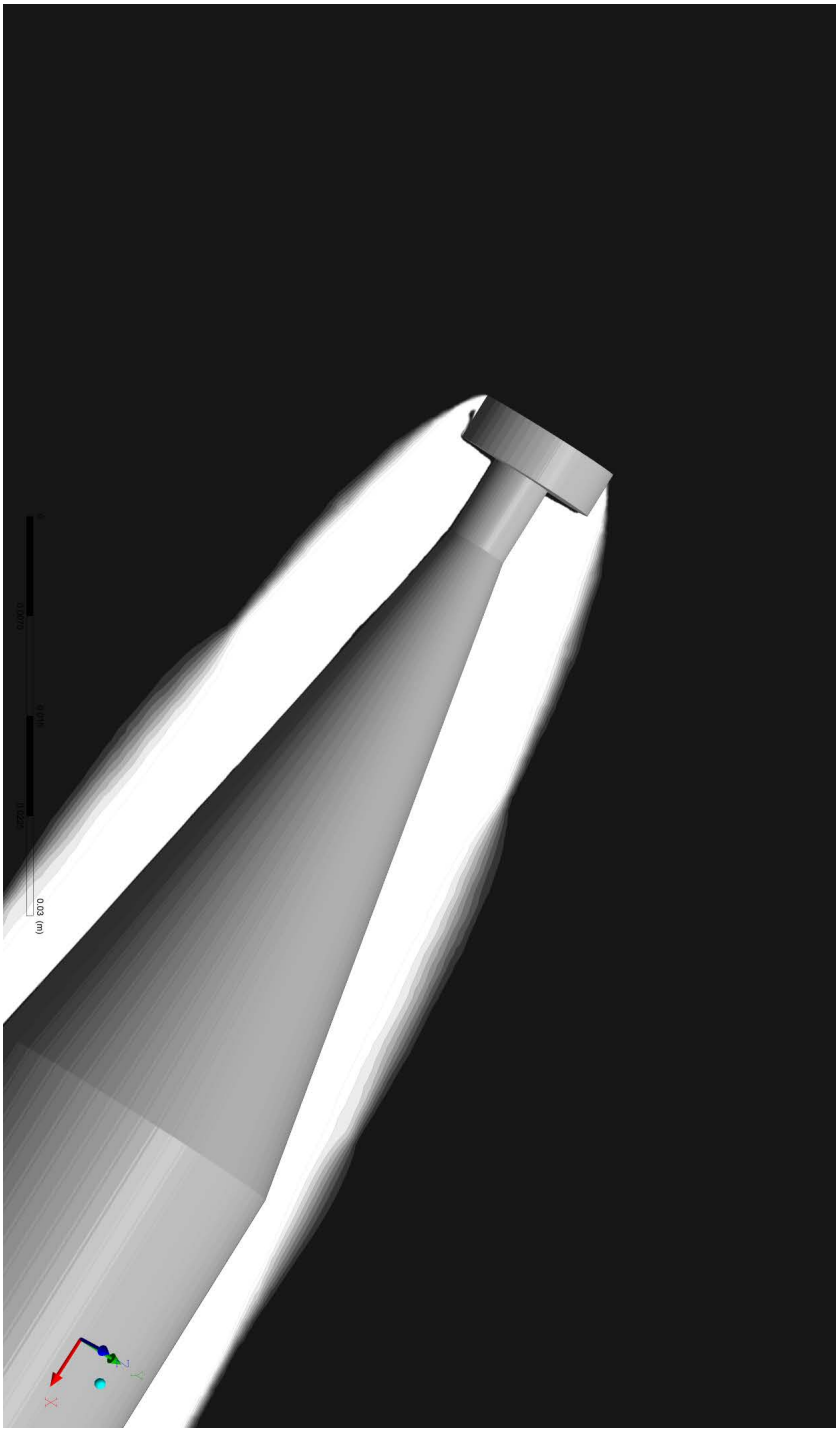

Figure 6.1: The new cavitating geometry.

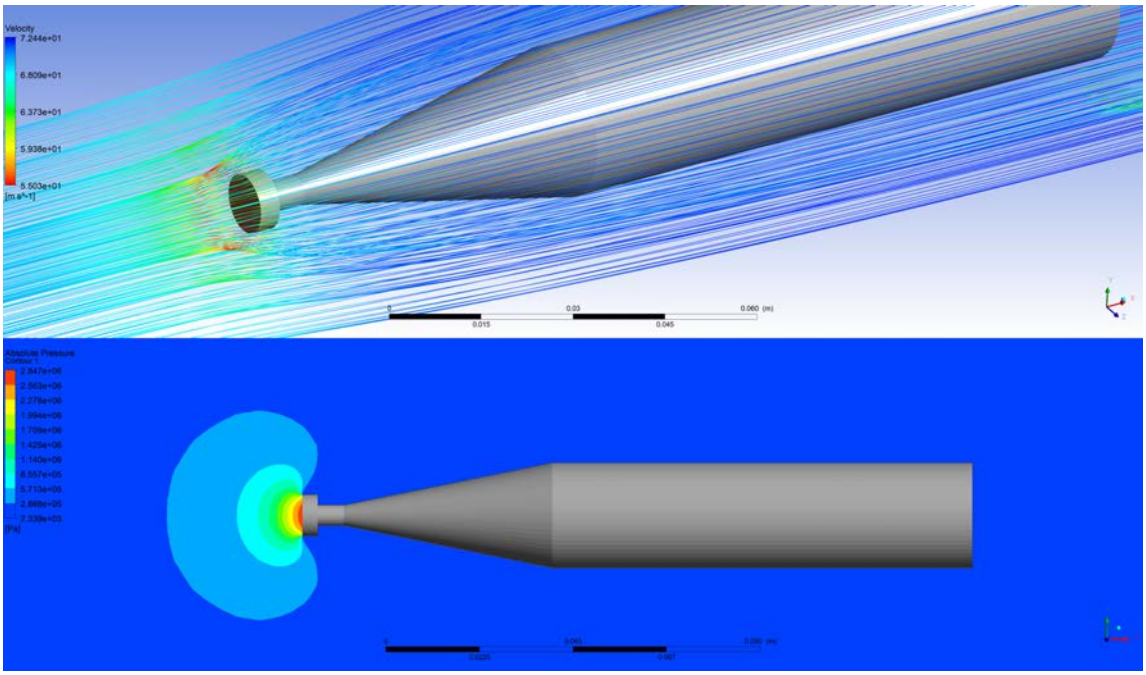

Figure 6.2: Streamline velocity and pressure around the new profile.

vapor cavity covers the whole body reducing pressures behind this. It means that it's like geometries move entirely in air.
This is an achievement for two reasons:

- first of all, it has been possible to have a drag reduction without using ventilated cavities;
- secondly, we understand that designing these geometries is extremely delicate. Indeed a single mm completely changes efficiency.

In spite of that, simulations continued testing the same model at different speeds. The results showed an absolutely encouraging behaviour for future developments, but not acceptable for our purpose. we began with a 40.55 m/s speed, that is too high to have a c_d higher than 0.3.
In this case, cavity envelopes the whole torpedo only in the first moments. During the next, analysing both c_d and cavitation bubble over time, it is leading the cloud

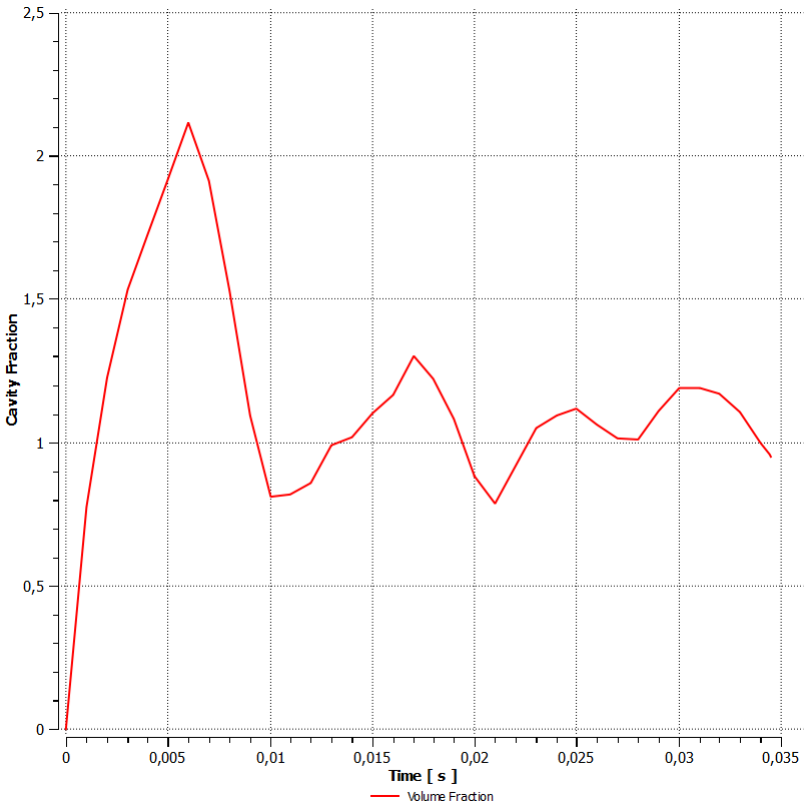

Figure 6.3: Periodic oscillation of the cavity length.

cavitation phenomenon(figure 6.3).

Vapour volume fraction oscillates between two values, which is not a problem in simulation environment but it do involve severe disadvantages in real life: sudden changes of cavity conditions can cause overpressures that could make the drag rise further. The easiest way of solving this might be to increase the cavitator diameter, but the first simulations show that it is associated with a drag rise making the hydrodynamics performances worse.

The last simulation was conducted at 22.15 m/s.

Even here, we can see that it is established a periodical partial cavitation in which c_d fluctuates between 0.35 and 0.5 with a period of about 4ms. However, these values may be accepted even if they are much higher than the 0.2 hypothesized, with

the consequence loss of efficiency at low speeds. But in this preliminary stage will be given wide coverage to lowering drag in the transition between non-cavitating and supercavitating conditions, shifting the problem to speeds between 35m/s and 55m/s for which high drag coefficients translate into almost unattainable thrusts.
Even if it is not presented in this thesis, a new project for a three-phase simulation has already been started in order to add a ventilation system to encourage cavities formation.
We are sure, that this will take the design to achieve the desired results.

7 Conclusions

In conclusion, we answer the questions raised in the introduction:

- is it possible to establish supercavitation starting at v=0m/s?
  Our studies show that using supercavitating profiles implies low efficiency at low speeds respect to other geometries (i.e. such as ogive heads), but this issue can be treated increasing thrust at these velocities. Nevertheless, increasing speed there comes a point which, reaching supercavitation is fundamental in order to keep low drags. We assume that there is an insuperable limit (about 40kn) beyond which our engine cannot guarantee sufficient thrust for overcome drag in non cavitating conditions.
  Despite that, the answer is yes if we create cavities using ventilated cavitation, in order to increase efficiency and therefore decrease c_d. The main advantages consist of reducing both speed range in transitional phase between non-cavitating and supercavitating conditions (high c_d) and the velocity at which supercavitation is reached.

- are there any possible developments on the model that can be made?
  Such as we have seen so far, there are two practical ways we can go. The first is to develop a model apt to the study of temporal phenomena, the second is to validate a three-phase model adding gas injectors. We suggest the second choice if the aim is to design a new propulsion system, warning that 3D simulations will be needed. For research purpose, LES model is our first choice in order to capture temporal variations but we do not expect any dramatic new discoveries able to increasing efficiency.

- what are the further potentials to be developed in a future work?
  Studying cavitation and supercavitation is useful in reducing drag, but there

are advantages and disadvantages that have to be analysed in order to design high-speed underwater vessels. Clearly using gas injectors is one of the common strategies that has been studied over years, but we want to introduce a new idea that hopefully will be developed in future studies: engine nozzles that cavitate in order to create stable cavities on their walls. This could bring two benefits:

- drag reduction due to lowering pressures on nozzle walls;
- they could be considered as adaptive nozzles which change their characteristics with speeds.

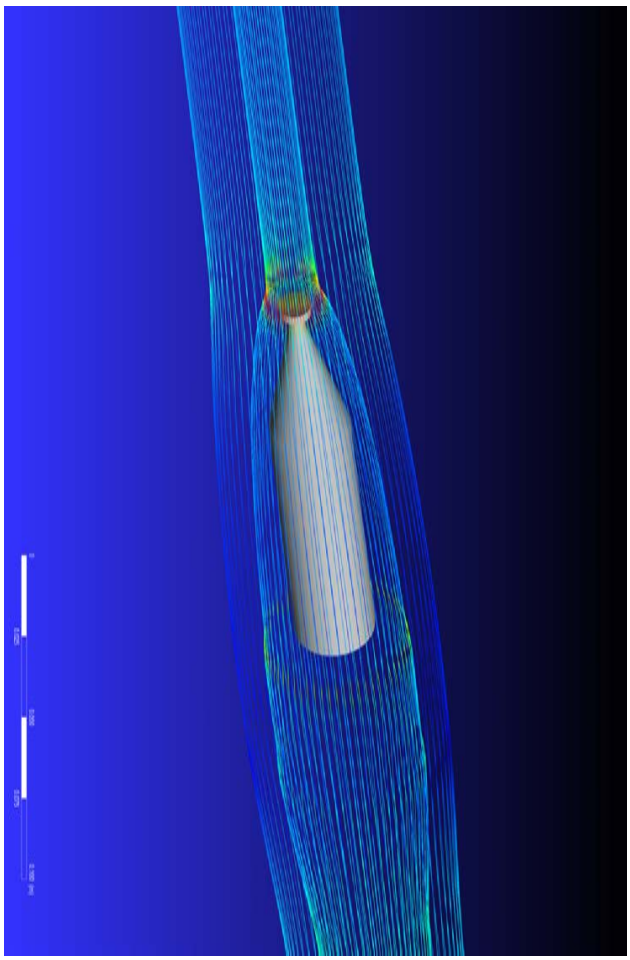

References

[1] Jean-Pierre Franc and Jean-Marie Michel (Eds.): *Fundamentals of Cavitation* New York, Boston, Dordrecht, London, Moscow, Kluwer Academic Publishers, 2004

[2] X.F. Guo, D. Yang, Y.L. Xiong: *Drag Reduction of a Rapid Vehicle in Supercavitating Flow* International of Naval Architecture and Ocean Engineering 9 (2017) 35-44

[3] Jiyusn Tu, Guan-Heng Yeoh, Chaoqun Liu: *Computational Fluid Dynamics* Butterworth-Heinemann, 2018

[4] Ali et al.: *Optimal Mesh Topology Generation for CFD* School of Mechanical and Manufacturing Engineering, National University of Sciences and Technology, H-12, Islamabad, Pakistan.

[5] Hunter Rouse and John S.McNown: *Cavitation and Pressure Distribution* Iowa Instituto of Hydraulic Research, Iowa City, 1948

[6] ANSYS FLUENT Tutorial Guide. Release 14.5. ANSYS, Inc. October 2012

[7] Robert F. Kunz David A. Boger Thomas S. Chyczewski David R. Stinebring Howard J. Gibeling: *Multi-phase CFD Analysis of natural and ventilated cavitation about submerged bodies* Proceedings of FEDSM '99 3rd ASME/JSME Joint Fluids Engineering Conference July 18-23, 1999, San Francisco, California

[8] Igor Nesteruk: *Supercavitation, Advances and Perspectives* A collection dedicated to the 70th jubilee of Yu.N.Savchenko, Springer, 2012

[9] Mohsen Y. Mansour1, Mohamed H. Mansour, Nabil H. Mostafa and Magdy Abu Rayan: *Comparison Study of Supercavitation Phenomena on Different Projectiles Shapes in Transient Flow by CFD* The International Conference of Engineering Sciences and Applications, Aswan, Egypt, January, 29 – 31, 2016

[10] M.S. Seif et al. *Drag force on a flat plate in cavitating flows* Sharif University of Technology, POLISH MARITIME RESEARCH 3(61) 2009 Vol 16; pp. 18-25 10.2478/v10012-008-0028-2

[11] http://www.pointwise.com/yplus/

[12] Lucian Hanimann, Luca Mangani, Ernesto Casartelli, Matthias Widmer :*Steady-state cavitation modeling in an open source framework: Theory and applied cases* ISROMAC 2016 International Symposium on Transport Phenomena and Dynamics of Rotating Machinery Hawaii, Honolulu April 10-15, 2016

[13] https://www.scmp.com/news/china/article/1581476/breakthrough-chinese-scientists-supersonic-submarine-technology-played

[14] https://en.wikipedia.org/wiki/

[15] Tucker, Paul G.: *Computation of Unsteady Internal Flows* Fundamental Methods with Case Studies, Springer US, 2001